THESIS

ANALYZING RADIATION DEFECTS IN PHOTONIC INTEGRATED CIRCUITS

Submitted by

Kevin Mienta

Department of Electrical and Computer Engineering

In partial fulfillment of the requirements

For the Degree of Master of Science

Colorado State University

Fort Collins, Colorado

Fall 2025

Master's Committee:

Advisor: Mahdi Nikdast
Co-Advisor: Biswajit Ray

Michael Mooney

ABSTRACT

ANALYZING RADIATION DEFECTS IN PHOTONIC INTEGRATED CIRCUITS

This thesis aims to address the challenges in analyzing the performance of silicon photonic integrated circuits under radiation effects. Silicon photonic integrated circuits (PICs) are increasingly being explored for next-generation optical communication systems in both near-Earth and deep-space missions. This growing interest stems from the rising demand for high-throughput data links—potentially reaching terabit-per-second rates—alongside the pressing need to reduce size, weight, power consumption, and cost (SWaP-C). As missions push further into harsh space environments, it becomes critical to evaluate the impact of space radiation on the performance and reliability of PICs. Physically developing and analyzing PIC performance in radiation-harsh environments is a long and expensive process. A radiation-aware design-space exploration and simulation framework, called RADPIC, was developed to analyze the performance of PICs under radiation effects. RADPIC consists of optical and electrical analyses and simulations that consider the impact of total ionizing dose (TID) on silicon-on-insulator (SOI) based PICs. As a case study, the performance (e.g., frequency response, extinction ratio, Quality-factor) of a microring resonator modulator (MRM) was analyzed under radiation exposure. The results are compared with previously reported experimental data and demonstrate good agreement. RADPIC lays the foundation for developing radiation digital twin models, enabling enhanced performance and radiation hardness of PICs for space missions.

ACKNOWLEDGEMENTS

I would like to thank my advisor Mahdi Nikdast and my co-advisor Biswajit Ray for all of their efforts in guiding and teaching me the research process during my time being their student. All of my questions and concerns were answered in our weekly meetings which helped ensure that my thesis stayed on the right track and progress was being made. I would also like to thank Amin Shafiee for his assistance in working through difficulties I faced in my simulations. Lastly, I would like to thank my friends and family for their support throughout my pursuit of higher education.

DEDICATION

I would like to dedicate this thesis to my family.

TABLE OF CONTENTS

LIST OF TABLES

LIST OF FIGURES

Chapter 1

Introduction

1.1 Problem Statement and Motivation

Silicon photonic (SiPh) devices and photonic integrated circuits (PICs) show much promise in meeting the demands of various applications, specifically in space. Space applications like near-Earth and deep-space communication (Figure 1.1) are one of the exciting areas for SiPh devices and PICS because of the advantages in bandwidth, size, weight, power consumption, and cost (SWaP-C). Due to these benefits, namely size and weight, satellites can fit smaller communication systems on board with room for more scientific experiments, or keeping the same footprint, they can have more powerful systems. Organizations like NASA's Jet Propulsion Laboratory (JPL) have been trying to utilize these advantages in communication systems in their Deep Space Optical Communications (DSOC) program [4]. Advancements in optical space communication are crucial in supporting the new space economy, which will not only involve governments but also the private sector. There has been an increased interest in space tourism, asteroid mining, and climate change monitoring [5]. The success of these optical space systems, mainly comprised of PICs, depends on how well some key challenges are addressed. These challenges include radiation hardness, thermal stability, reliability, and longevity [6]. Experiments aimed at addressing these challenges have already begun. Space qualifying tests for PICs have already begun on the International Space Station (ISS) with promising performance demonstrated in low Earth orbit [7]. PICs have also been of great interest in other applications, other than space, such as high-energy physics (HEP) applications. These HEP applications can require PICs to withstand harsh radiation environments. Specifically, the European Organization for Nuclear Research (CERN) is considering using PICs in the Large Hadron Collider (LHC) to deal with ever-increasing data traffic demands [1]. As these optical systems become increasingly popular, the need for radiation-hard PICs will continue to grow. Running experiments, such as placing PICs in low Earth orbit, can be very costly. The

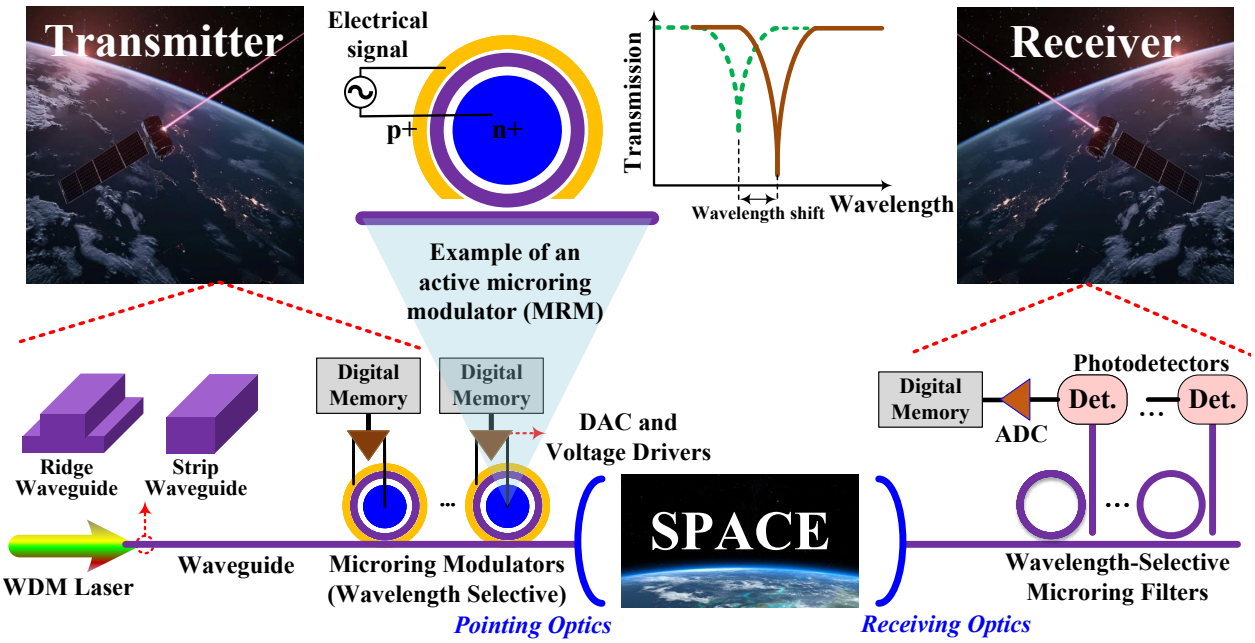

Figure 1.1: An example of optical communication in space with PICs. Top: Example of MRM with its optical spectrum (right). The various components of a PIC are present, including a laser, waveguides, modulators, and photodetectors.

design of SiPh devices in PICs varies greatly to enhance performance for specific applications. Extensive testing will be necessary to ensure that each new design is tolerant to radiation. In order to speed up research and development, the time for trial and error for device fabrication and testing needs to be reduced. The radiation hardness of a PIC is determined by many factors, such as geometries and doping levels [8] [2]. It is not ideal to iterate over many PIC designs through experimental testing because it is inefficient and costly. A simulation approach must be considered to tackle these challenges. Specifically, there is a strong need for a radiation-aware design space exploration framework.

1.2 Thesis Organization

The thesis is organized into the following chapters. Chapter 2 discusses the background of integrated photonics, the underlying physical principles, and high-energy radiation effects. Chapter 3 discusses how radiation affects SiPh devices and how radiation effects can be simulated on active SiPh devices in RADPIC, the novel contribution of this thesis. Chapter 4 provides a case study

for validating RADPIC, which applies RADPIC to an active SiPh device, followed by a discussion of the findings. Lastly, Chapter 5 focuses on future work needed to improve the accuracy and robustness of RADPIC.

Chapter 2

Background

2.1 Integrated Photonics

There are a few platforms that can be used for PICs. These include SiPh, indium phosphide (InP), and silicon nitride (SiN3). Of these, SiPh has shown the most promise due to its compatibility with complementary metal-oxide semiconductor (CMOS) technology. CMOS is the most popular semiconductor fabrication process for integrated circuits such as microprocessors and memory chips. This enables the creation of PICs with SiPh devices in existing foundries that have established processes, thereby minimizing development costs. One of the main processes for SiPh-based PICs is the silicon on insulator (SOI) technology, where the wafer consists of a silicon substrate as the base, then a layer of oxide (often referred to as the buried oxide layer), and a single-crystal silicon film. This structure provides the advantage of reduced capacitance and less susceptibility to radiation [9]. There is often also a top layer of oxide called the "cladding" that completes a PIC as shown in Figure 2.1. A typical wafer for SiPh devices has the silicon substrate at around 725 µm, 2 µm of buried oxide, and 220 nm of crystallized silicon as the top layer if no cladding is involved.

Beyond consideration of SWaP-C, the critical importance of SiPh includes the incredible data transfer speeds that can be achieved. SiPh transmitters have shown great performance with On-Off Keying (OOK) and pulse amplitude modulation with 4 levels (PAM-4)experiments in [10]. OOK is a two-level modulation scheme where data is sent as "on" or "off"; in this case, the light modulates between being on and off. PAM-4 has four different modulation levels encoding two bits of data. The authors demonstrated OOK tests with 182 Gbps and PAM-4 tests with 308 Gbps transmissions while achieving extremely high energy efficiency of 1 pJ/bit.

The author in [11] discusses how PICs can enable an order-of-magnitude increase in speed and energy efficiency in computation due to their analog nature. This can greatly accelerate the

Figure 2.1: The structure of an SOI wafer. There is a silicon base, followed by an SiO_2 layer, which insulates the following Si layer. Lastly, there is a cladding layer made from SiO_2 on top.

need for deep learning, which can be bottlenecked by the speed of digital circuits solving matrix multiplication computations. PICs, being analog, can perform these computations at light speed.

SiPh PICs can achieve such incredible performance because photons travel much faster than electrons [12]. Data sent using photons travels much faster than data sent using electrons, and therefore, PICs can operate at extremely fast data rates. Traditional electronic circuits utilize wires that allow for the flow of electrons and transistors that modulate that flow of electrons to transmit signals. PICs operate differently, using waveguides to transmit light, and components such as modulators and detectors manipulate that light to transmit signals as shown in Figure 1.1.

2.2 Waveguides

A waveguide is a structure specifically designed to direct and guide light, and it can be helpful to think of it as an optical wire. For light to be guided within a waveguide, it needs to experience total internal reflection, where the light stays confined within the waveguide. Total internal reflection stems from Snell's Law, illustrated in Figure 2.2, which is defined as:

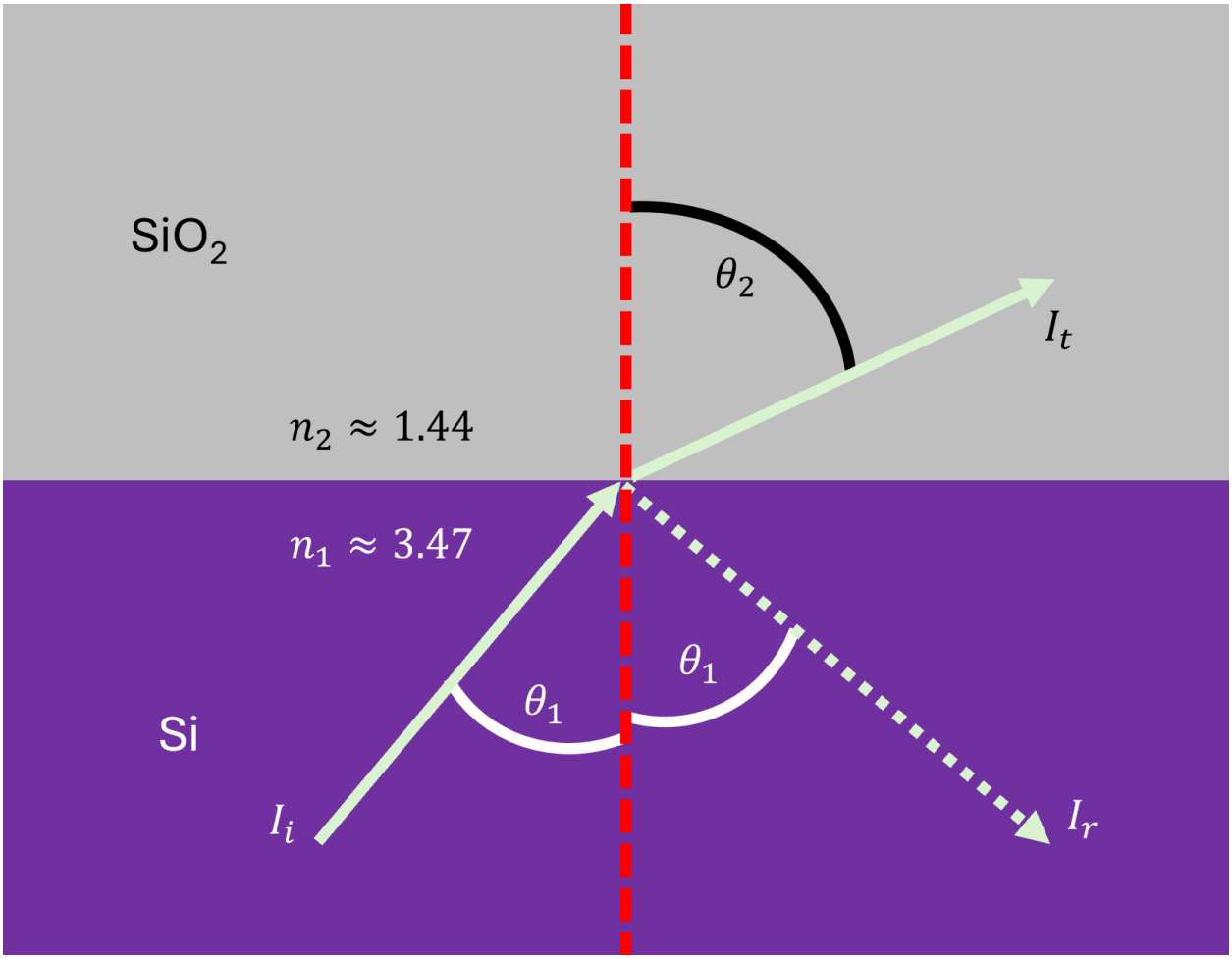

Figure 2.2: Snell's law illustrated with light (light green) entering from one medium to another, Si shown in purple and SiO_2 shown in gray. The refractive index values for materials are provided at 1550 nm wavelength.

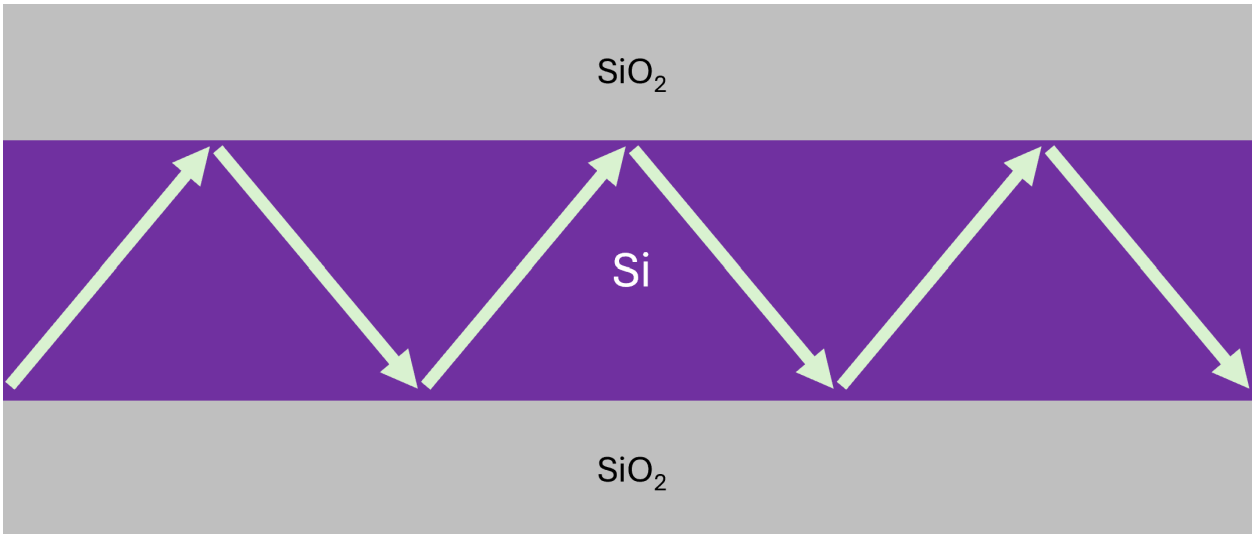

Figure 2.3: Total internal reflection in a waveguide shown with light (light green) entering a waveguide made from an Si (purple) waveguide and SiO_2 (gray) cladding.

$$n_1 sin(\theta_1) = n_2 sin(\theta_2) \tag{2.1}$$

where n_1 and n_2 are the refractive index of their respective materials, θ_1 is the incident angle of the light wave and θ_2 is the transmitted angle of the light wave. When θ_2 reaches an angle of 90 degrees θ_1 becomes the critical angle defined as:

$$sin(\theta_c) = \frac{n_2}{n_1} \tag{2.2}$$

where θ_c is the critical angle. For θ_1 values greater than θ_c, light is confined within the waveguide because there is no transmitted light ray escaping the waveguide, as can be seen in Figure 2.3.

The refractive index of a material is a dimensionless value defined as:

$$n = \frac{c}{v_p} \tag{2.3}$$

where c is the speed of light in vacuum and v_p is the phase velocity of monochromatic light in a medium. The refractive index describes how much light slows down when it enters a medium as compared to its speed in a vacuum. Waveguides are designed with materials that have favorable

refractive index values that make total internal reflection easily achievable. The most common waveguide materials are silicon (Si) and silicon dioxide (SiO_2). Si has a refractive index of around 3.47 at 1550 nm wavelength, and SiO_2 has a refractive index of around 1.44 at 1550 nm wavelength. The waveguide core, where the light travels, is made from a high refractive index material like Si, while the surrounding cladding is made from a low refractive index material such as SiO_2. This allows for (2.1) and (2.2) to be satisfied such that the light experiences total internal reflection and stays confined within the waveguide core.

A monochromatic plane wave traveling in space can be described as:

$$E = E_0 e^{i(\omega t - \beta x)} \tag{2.4}$$

where E is the electric field vector, E_0 is the amplitude of the electric field, ω is the angular frequency, t is time, and β is the propagation constant. β is defined as:

$$\beta = \frac{2\pi n}{\lambda} \tag{2.5}$$

where n is the refractive index and λ is the wavelength of light. β describes the change in the phase of the light wave as it travels through a medium.

Within the waveguide, light waves travel in distinct patterns known as optical modes, which are solutions to Maxwell's equations that govern the behavior of light. Light consists of alternating electric and magnetic fields, and when the electric field is traveling transverse to the direction of propagation and is parallel to the wafer surface, the light has a transverse electric (TE) polarization. If the magnetic field is behaving in the same way, then the light has transverse magnetic (TM) polarization. An optical mode is transverse polarized light that travels along the waveguide with a constant amplitude and polarization. Waveguides are designed with the intent of guiding specific optical modes. The two common waveguide designs are strip and ridge waveguides. The strip waveguide is a Si structure with no base, unlike the ridge waveguide, which has the waveguide core placed on a Si base as illustrated in Figure 2.4. For both waveguides, the portion of

the mode's electromagnetic field that extends beyond the waveguide structure into the surrounding medium is called the evanescent tail. This wave does not propagate away from the waveguide, and it exponentially decays. The degree to which the evanescent tail extends out past the waveguide is wavelength-specific. Waveguides' geometries are chosen to optimize optical performance, fabrication cost, and design constraints.

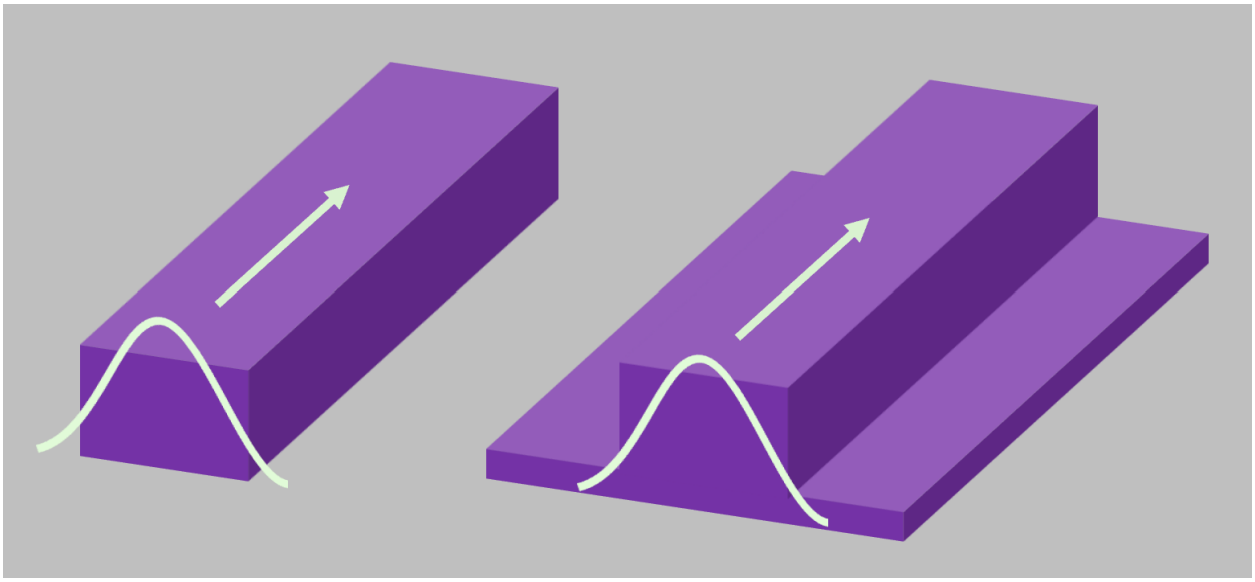

Figure 2.4: On the left, the mode is illustrated by the light green wave propagating in the direction of the arrow in a strip waveguide. On the right, the mode is propagating in a ridge waveguide.

The geometry of a waveguide, the medium of the waveguide core, and its surroundings all impact the way that the optical mode travels down the waveguide. Instead of using the refractive index, n, a term called the effective index is used. n_{eff} defined as:

$$n_{eff} = \frac{\beta\lambda}{2\pi} \tag{2.6}$$

where β is the propagation constant of the mode and λ is the wavelength of light. n_{eff} is used to describe the phase velocity of the mode.

In reality, an optical mode consists of a narrow range of frequencies centered around the desired central frequency, such as 1550 nm. These frequencies, superimposed together, create a wave

packet that has an overall shape or envelope. This envelope is what carries information in a light wave, or mode, through a waveguide. To describe how the mode propagates in a waveguide, the group index is used, and it is defined as:

$$n_g = \frac{c}{v_g} \tag{2.7}$$

where v_g is the speed of the envelope of the optical mode.

Many optical modes can be present in a waveguide; however, not all are guided modes. In Figure 2.5 and Figure 2.6, higher-order TE modes were simulated, in 2D, for a strip and ridge waveguide, respectively. Both waveguides share a similar geometry of being 500 nm wide and the core being 220 nm tall; however, the ridge waveguide has the added slab region underneath that is 100 nm tall. The electric field is plotted with normalized intensity. Both waveguides have the majority of the electric field intensity centered in the waveguide, illustrating a guided mode. For the higher TE modes, the electric field intensity starts leaking out, showing increasingly unguided modes from TE mode 2 to TE mode 3. It is important to note that 2D waveguides do not have pure TE or TM modes but rather have quasi-TE or quasi-TM modes. This means that the electric or magnetic field is not perfectly polarized in the transverse direction. The degree to which the electric (or magnetic) field is polarized in the transverse direction is how modes are organized, with the fundamental TE or TM mode having the highest polarization in the transverse plane, while the higher-order modes have increasingly less polarization.

2.3 Modulators

In SiPh, devices that can modulate the intensity of optical signals are called modulators. The two most common modulators are the Mach-Zehnder Modulator (MZM) and the microring resonator modulator (MRM). MZMs are active, optoelectronic devices that modulate optical signals by utilizing the interference between a split optical signal beam with one or both experiencing a phase shift. MRMs are also active, optoelectronic, wavelength-selective devices that modulate

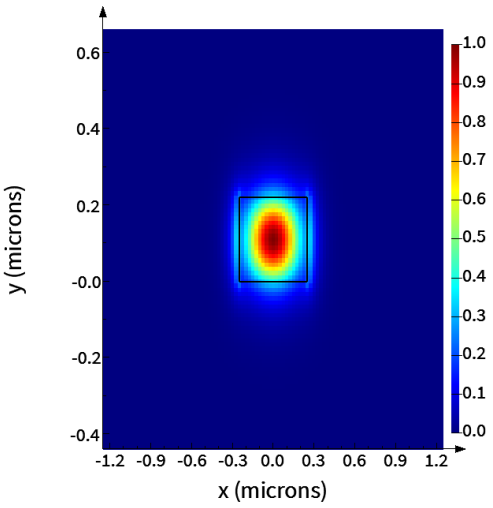

(a) TE Mode 1

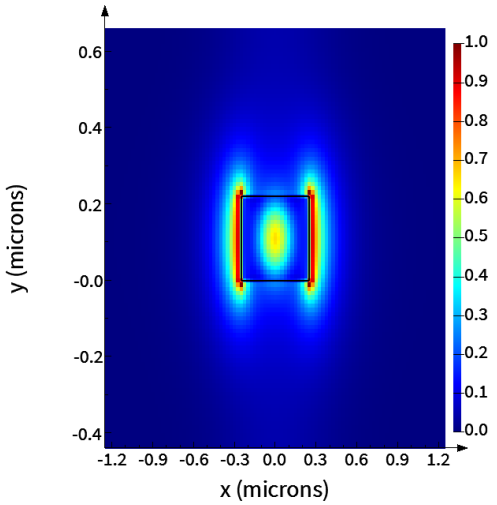

(b) TE Mode 2

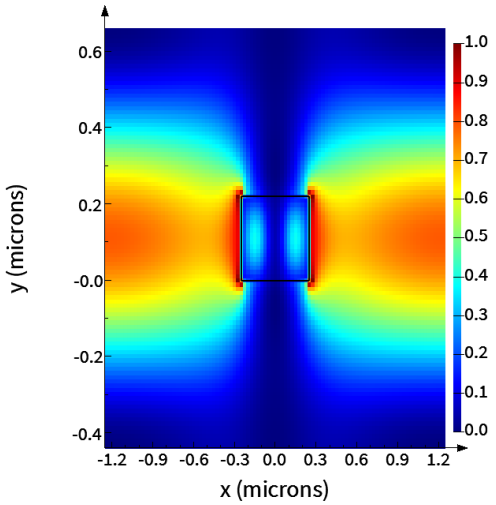

(c) TE Mode 3

Figure 2.5: TE modes profiles within a strip waveguide, the structure superimposed with black borders, with the color bar representing normalized electric field intensity. (a) The first TE mode has its electric field intensity mostly centered in the waveguide, which exemplifies a guided mode. (b) For the second TE mode, most of the electric field intensity is still centered in the waveguide, but with much less amplitude, and parts of the mode are not contained in the waveguide. (c) The third TE mode is almost completely unguided, with most of its electric field intensity outside the waveguide.

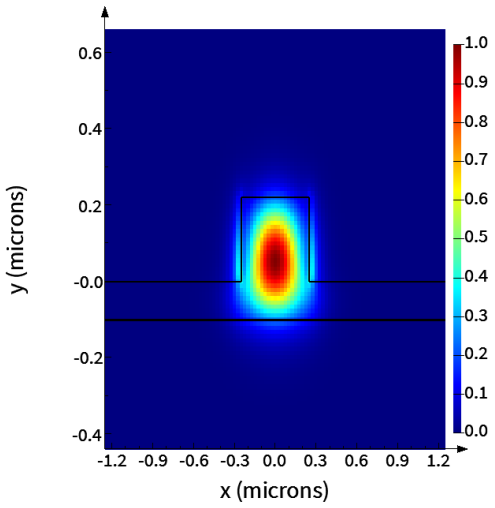

(a) TE Mode 1

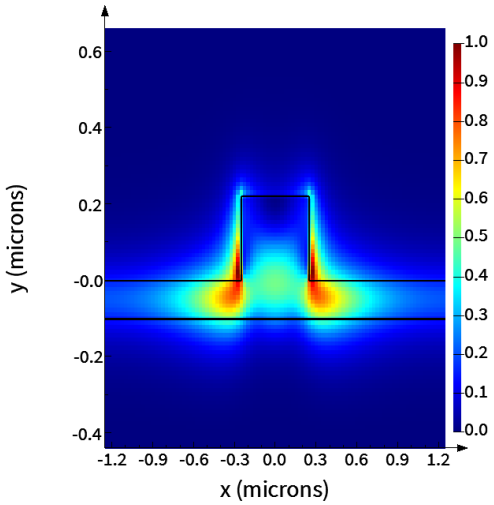

(b) TE Mode 2

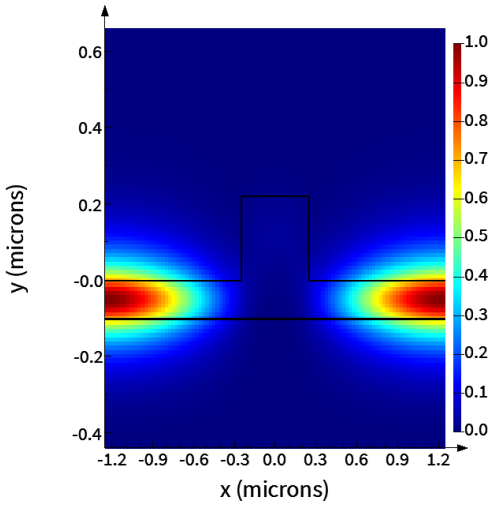

(c) TE Mode 3

Figure 2.6: TE mode profiles within a ridge waveguide, the structure superimposed with black borders, with the color bar representing normalized electric field intensity. (a) The first TE mode shows a guided mode centered in the waveguide. (b) The second TE mode shows most of the electric field intensity present in the slab region on the sides of the waveguide core, with the waveguide core retaining some field intensity. (c) The third TE mode has no guided mode within the waveguide, and the electric field intensity is mainly focused in the slab region on the sides of the waveguide core.

optical signals that utilize resonance-induced interference within a microring waveguide. Both of these devices are widely used in high-speed optical communication. The MZM originates from the Mach-Zehnder Interferometer (MZI), illustrated in Figure 2.7. An MZI is a device that measures

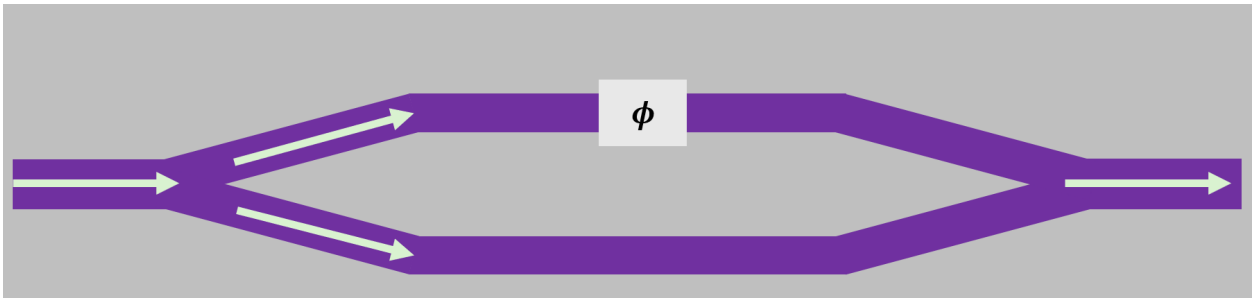

Figure 2.7: A MZI illustration. The light green arrow depicts light entering the MZI. The light splits down each arm of the MZI, with one of the light beams experiencing an arbitrary phase shift. The two light beams recombine at the end of the MZI with their modified phases affecting the output light intensity.

the relative phase shift of an optical signal split into two beams from one source. Any imbalance in the light paths will result in a relative phase shift, resulting in a change in the output light intensity at the output of the MZI. The interference can be destructive, constructive, or any amplitude in between. Assuming an MZI with negligible losses, the output intensity is governed by:

$$I_o = \frac{I_i}{2}[1 + cos(\beta_1 L_1 - \beta_2 L_2)] \tag{2.8}$$

where I_o is the output intensity of the MZI, I_i is the input light intensity, β_1 and β_2 are the propagation constants of the two separate arms, and L_1 and L_2 are the lengths of the two separate arms [13]. A relative phase shift between the arms can be enacted by a change in the length between the two arms or a change in the propagation constant of one of the arms. To create an MZM, the imbalance in the light on one or both of the paths is carefully controlled by using an active phase shifter. An active phase shifter would modify the effective index, which, from (2.5), would modify the propagation constant, β.

A MRM originates from a microring resonator (MRR), illustrated in Figure 2.8. An MRR device consists of a circular waveguide, the microring, with one or two straight waveguides posi-

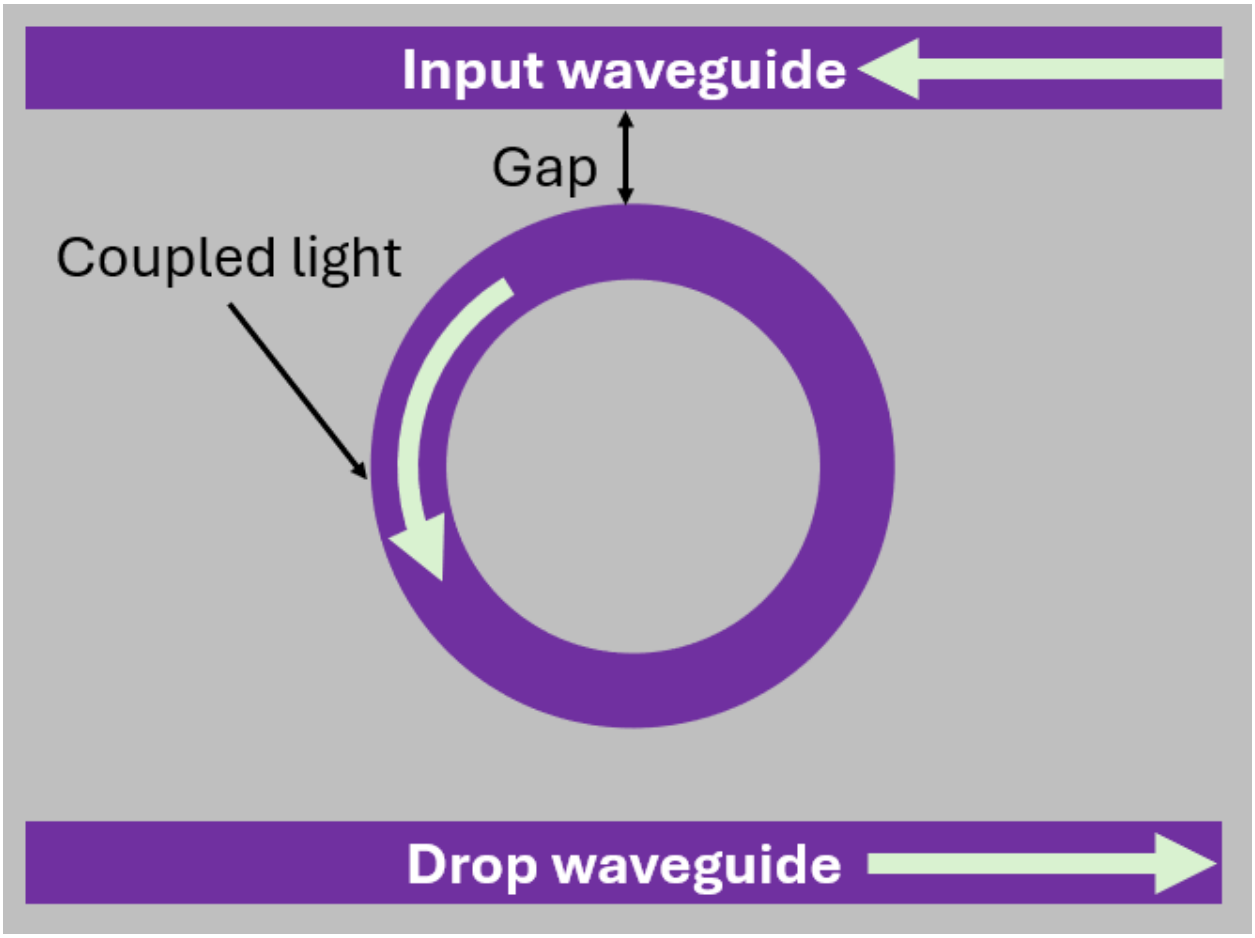

Figure 2.8: MRR structure showing an input waveguide, drop waveguide, and a ring in the center, all made from Si (purple) and SiO_2 (gray) cladding. When the MRR is on resonance, light (light green arrow) couples from the input waveguide into the ring and couples from the ring into the drop waveguide.

tioned adjacent to it. When only one waveguide is present (the input waveguide), this is referred to as an all-pass resonator. In the all-pass structure, when an optical signal propagates through the input waveguide that is adjacent to the ring at a specific wavelength, the resonant wavelength will couple into the MRR microring, dropping it from the input waveguide. When the MRR consists of two waveguides, the second waveguide, positioned opposite to the input waveguide relative to the microring, is called the add-drop waveguide. In the add-drop configuration, resonant wavelengths that are dropped from the input waveguide couple to the drop port of the add-drop waveguide. This allows for the resonant wavelength that was filtered out of the input waveguide to be further rerouted for processing. An optical signal at the resonant wavelength enters the microring due to resonant coupling. When an optical signal at the resonant wavelength travels down the input waveguide, the evanescent tail of the mode extends into the microring waveguide, allowing for the optical signal to couple into it.

When the round-trip optical phase in the MRM constructively interferes at the resonant wavelength, the optical signal is effectively dropped from the input waveguide. The optical phase is defined as:

$$\phi_{rt} = \frac{2\pi n_{eff} L_{rt}}{\lambda} \tag{2.9}$$

where ϕ_{rt} is the round-trip phase of the optical signal, λ is the wavelength of the optical signal, n_{eff} is the effective index of the MRR, and L_{rt} is the round-trip length of the optical path. For an MRR with radius r, L_{rt} is defined as $2\pi r$. When the round-trip optical phase is an integer multiple of 2π, the optical phase constructively interferes within the MRM, and resonant coupling occurs, also called a resonant mode. Therefore, the resonant wavelength is defined as:

$$\lambda_{res} = \frac{n_{eff} L_{rt}}{m}, \tag{2.10}$$

where m is an integer value. The presence of this integer value results in many resonant wavelengths present throughout the optical spectrum. To create an MRM, the resonant wavelengths can be actively shifted by altering the optical properties of the microring.

Altering the optical properties of an MZM or MRM, for modulating optical signals, can be done with different approaches, but the most common ones include thermal tuning or modulating the carrier density in the devices. Specifically, the two arms in an MZM would be subject to modulation, and for the MRM, it would be the microring. The refractive index of the materials that these devices are comprised of, Si and SiO_2, is temperature dependent. Changing the temperature of these devices changes the effective index, which results in a modulated optical signal within microseconds [14]. Common materials for the heater include titanium, platinum, nickel, and chromium. When voltage is applied to the heater, the resulting current heats the heater material. This heat then transfers to the waveguide, altering its material properties and consequently affecting the effective index. An example of a heater placed in proximity to a waveguide is shown in Figure 2.9. The second approach is modulating the free carrier density in the MZM arms or the

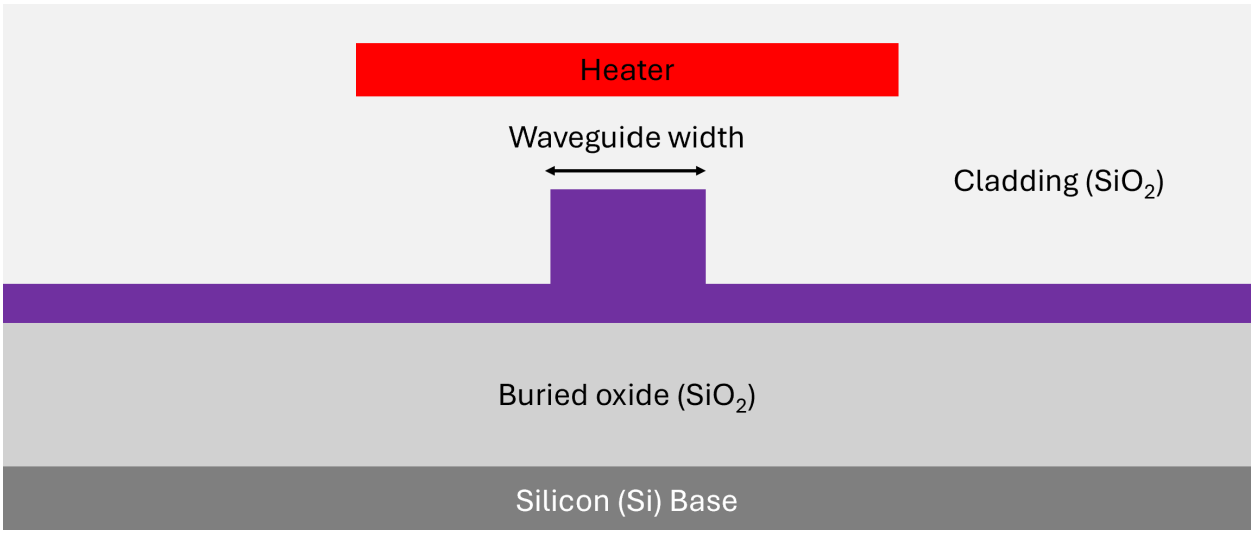

Figure 2.9: Heater, shown in red, placed over a waveguide.

MRM microring waveguide (as shown in Figure 2.10a and Figure 2.10b). The refractive index of Si can be altered through changes in the concentration of electrons and holes. If the waveguide is made from a p-n junction, applying a bias to that p-n junction modulates the majority carrier concentration, strongly affecting the effective index of the waveguide in nanoseconds [14]. The structure of a waveguide containing a p-n junction is shown in Figure 2.11. The change in the re-

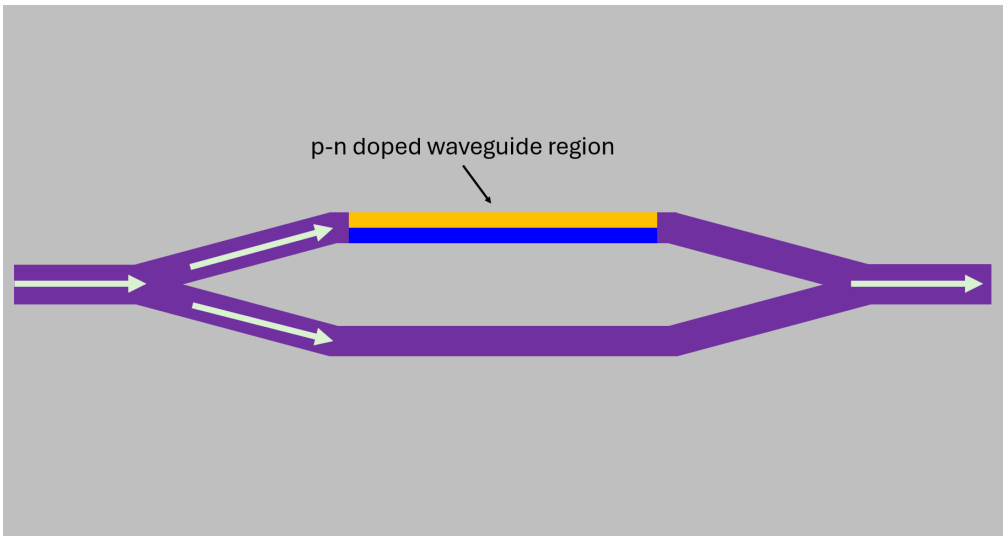

(a) MZM structure.

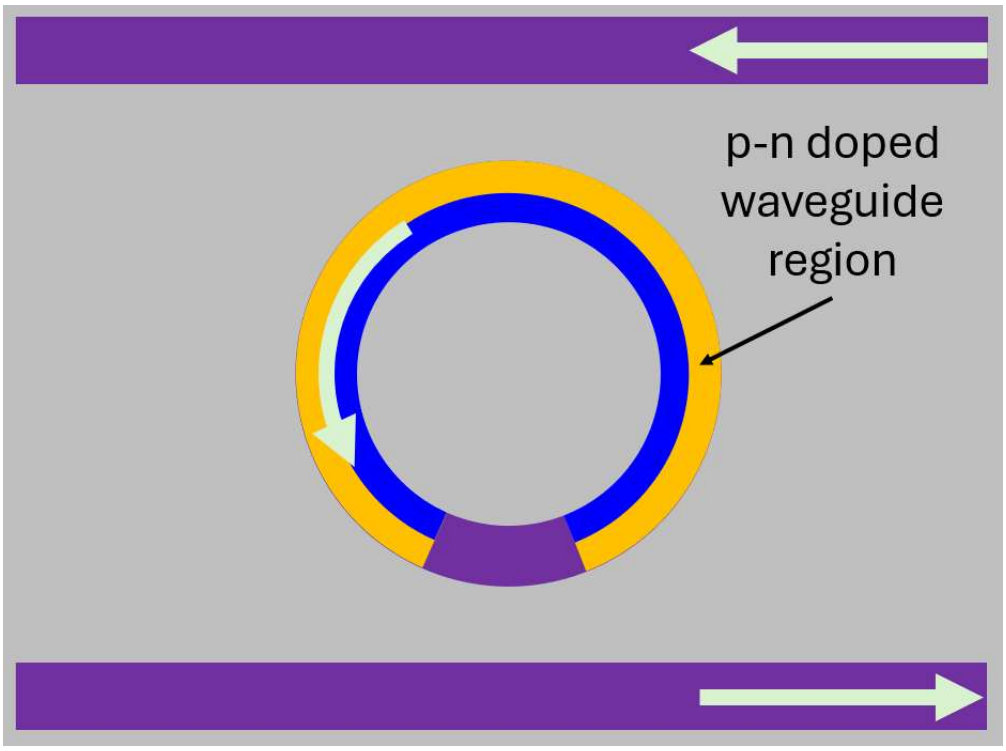

(b) MRM structure.

Figure 2.10: SiPh modulators that utilize a p-n junction as the modulation method.

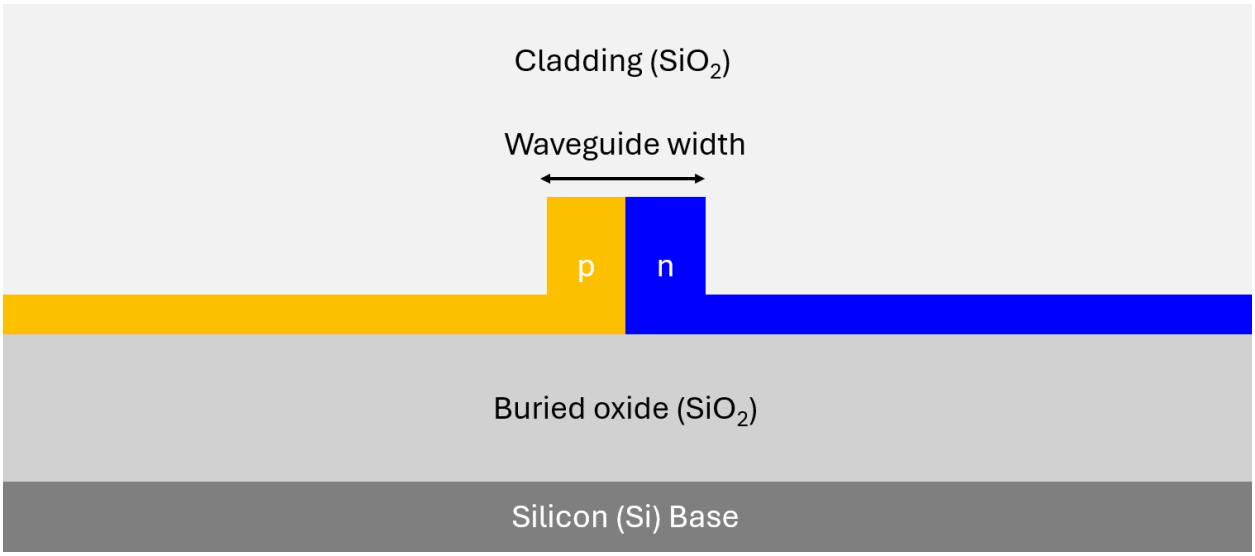

Figure 2.11: Ridge waveguide p-n junction cross-section.

fractive index due to the change in free carrier concentration is called the plasma dispersion effect. The plasma dispersion effect is defined by Soref and Bennett [15] as:

$$\Delta n = \frac{-e^2\lambda^2}{8\pi^2 c^2 \epsilon_0 n}[\frac{\Delta N_e}{m^*_{ce}} + \frac{\Delta N_h}{m^*_{ch}}]. \tag{2.11}$$

where, e is electron charge, c is the speed of light in vacuum, ϵ_0 is the permittivity of free space, n is the refractive index of the material, ΔN_e and ΔN_h are, respectively, the concentration of electrons and holes, m^*_{ce} is the conductivity effective mass of electrons, and m^*_{ch} is the conductivity effective mass of holes. In (2.11), the change in the refractive index of a material is proportional to the density of free carriers ΔN.

The discussion will now narrow its focus from discussing both the MZM and MRM to exclusively MRMs, as the remainder of this paper centers around their design, simulation, and analysis. The optical response of MRMs governs their performance characteristics for various applications, including high-speed optical communications. For an MRM, the transmission is usually measured at the output of the input waveguide. The MRM will encounter dips in its output transmission when it experiences a resonant mode. There are a few key parameters that can be extracted from the transmission spectrum that provide crucial insight into the MRM performance, as shown in Fig-

ure 2.12. The frequency spacing between resonant modes is called the free spectral range (FSR),

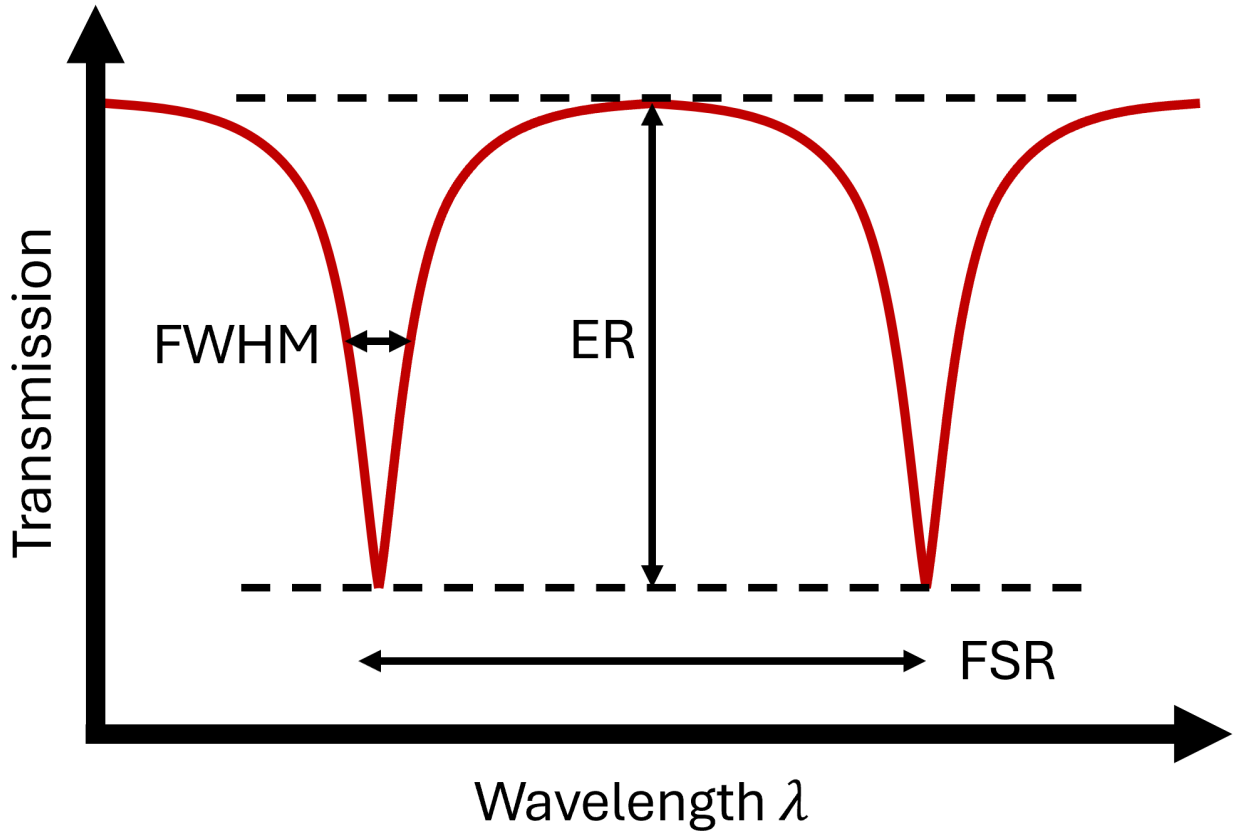

Figure 2.12: MRM optical response with FWHM, ER, and FSR shown.

and it is defined as:

$$FSR = \frac{\lambda_{res}^2}{n_g L} \tag{2.12}$$

where n_g is the group index of the MRM. The group index for an MRM is described as:

$$n_g = n_{eff} - \lambda_{res} \frac{dn_{eff}}{d\lambda_{res}} \tag{2.13}$$

where n_{eff} is the effective index of the MRM, λ_{res} is the resonant mode wavelength, and $\frac{dn_{eff}}{d\lambda_{res}}$ describes the change in the effective index with changing wavelength. The extinction ratio (ER) describes the difference between the maximum and minimum transmission levels for the resonant mode, quantifying the resonant dip. The full width at half maximum (FWHM) of the resonant

mode represents the spectral width of the resonance dip. It is measured at half the depth of the transmission minimum. The FWHM determines the Quality-factor (Q-factor) of an MRM, and it is defined as:

$$Q_{factor} = \frac{\lambda_{res}}{FWHM}. \tag{2.14}$$

The Q-factor describes the number of oscillations in the ring before the energy reaches $1/e$ of the initial energy [14], and impacts an MRM's modulation and bandwidth performance.

Modulating the resonant wavelength is the crucial function of an MRM. As discussed, thermal tuning and the plasma dispersion effect are both mechanisms by which this modulation can take place. An important performance parameter to consider is the modulation efficiency of an MRM. The modulation efficiency is the measure of the shift in the resonant wavelength against an applied voltage. (e.g. 1 V). The applied voltage changes the free carrier density in the MRM, dynamically changing the resonant mode. One consequence of increased free carrier density is the increase in the absorption of light within the silicon waveguide [14]. This results in a decrease in the Q-factor of the MRM. The change to the Q-factor will move the MRM away from its resonant mode, which also reduces the ER [14].

2.4 High Energy Radiation Effects

Radiation effects on PICs are a crucial topic that needs to be addressed thoroughly for the long-term success of PICs in radiation-hard environments. The following discussion covers the basic mechanisms of radiation on materials with a more focused discussion of radiation effects on PICs in Chapter 3.

There are three main types of radiation effects: total ionizing dose (TID), displacement damage dose (DDD), and single event effect (SEE) [1]. TID is the cumulative amount of ionizing radiation absorbed by a material. DDD described the damage caused by incident particles colliding with the crystal lattice of a material, creating defects in the material structure due to the displacement of atoms. SEE occurs when a high-energy particle penetrates through a material, inducing charge generation. The three radiation effects are compared in Table 2.1. Radiation effects such as TID

are discussed in [16]. TID can lead to charge generation in a material due to the energy absorbed from ionizing radiation. A single high-energy particle, such as a photon, electron, or proton, can create large numbers of electron-hole pairs and, free carrier density. Since electrons have a higher mobility than holes, they quickly escape from the material. The free holes have lower mobility and have a higher probability of recombining back into the material. The fraction of holes that escape recombination is described in [16] as:

$$N_h = f(E_{ox}) g_0 D t_{ox}, \tag{2.15}$$

where $f(E_{ox})$ is a fraction scalar that relates the electric field in the oxide to the hole yield. g_0 is the ionization constant of the material representing electron-hole pair density per rad of dose per unit volume, D is the radiation dose, and t_{ox} is the thickness of the oxide. $f(E_{ox})$ is based on the electric field strength in the oxide. For gamma (Co-60) radiation, $f(E_{ox})$ is roughly 1 under extreme radiation, and for 10 keV X-rays, $f(E_{ox})$ is around 0.8.

Table 2.1: High Energy Radiation Effects. Content from [1]

Damage Effects	**TID**	**DDD**	**SEE**
Radiation particles	Alpha, Beta, Gamma	Alpha, Beta, Gamma, Neutron	Alpha, Beta, Gamma, Neutron
Time to recover	Extended	Extended	Transient
Damage mechanism	Local field modulation driven by charge generation	Displacement in lattice structure driven by collisions	Carrier population increase driven by charge generation
Microscopic defects	Surface oxidation, increased carrier population, bulk trapped charges	Material point defect, carrier recombination center	carrier population increase
Macroscopic Effects	Refractive index shift, absorption increase, conductivity modulation	Volume increase or decrease, absorption increase	transient current surge

To study ionizing particle radiation in SOI materials, The Stopping Range of Ions in Matter (SRIM) [17] can be used. This tool was used to model how alpha radiation affects Si and SiO_2 at very high energy levels. In Figure 2.13, the alpha radiation penetrates Si more than SiO_2, especially at higher energy levels. This tool can provide insights into the recommended depth

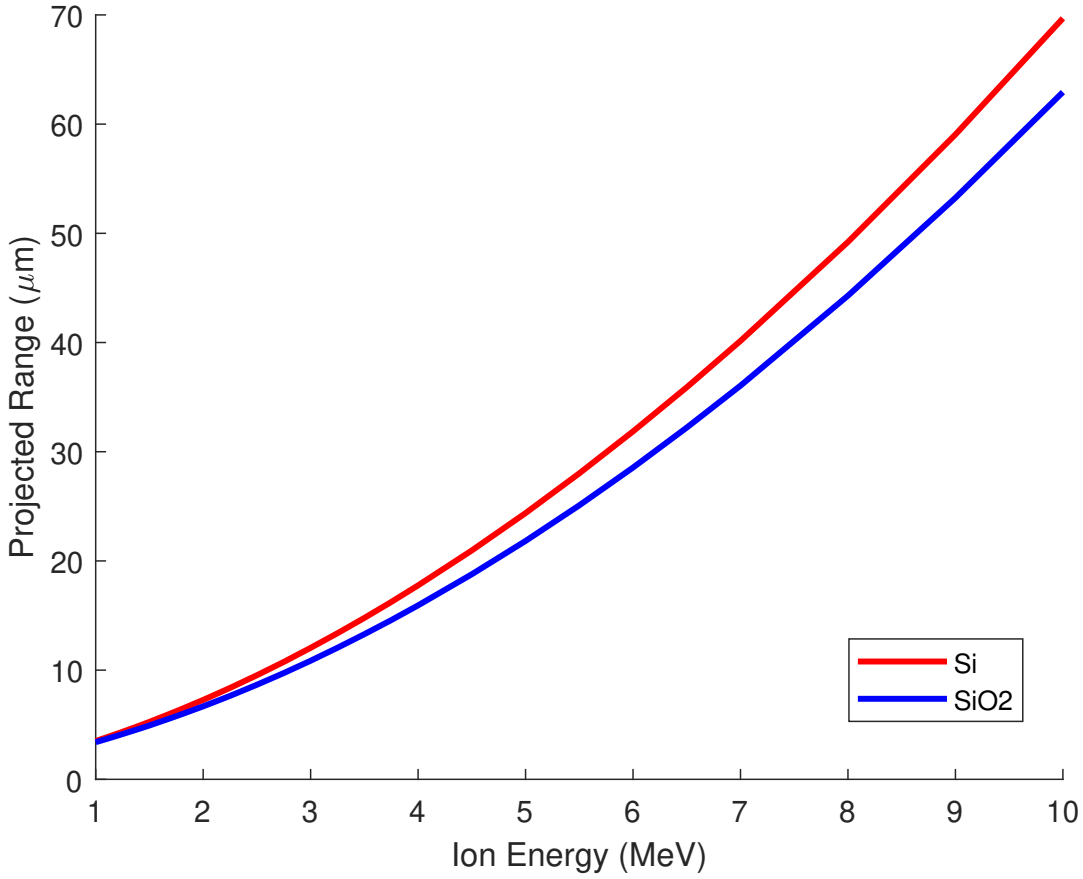

Figure 2.13: Projected range of alpha radiation within Si and SiO_2. Particle energy shown from 1-10 MeV.

of various layers in an SOI device. The SRIM software also includes The Transport of Ions in Matter (TRIM) tool. This tool models detailed interactions of ions with a target material. Two TRIM simulations were performed with He ions of 1 MeV of energy as the source, one for Si as the target, and one for SiO_2 as the target. Each TRIM simulation included modeling of collision events, ion penetration depth, and ionization. In Figure 2.14a, the most collisions occur around 3 to 3.5 µm deep into the Si. The location of these collision events matches the projected ion range

of 3.5 µm in Figure 2.14c. The ionization shown in Figure 2.14b shows the energy loss of ions to the target material's electrons. The most energy loss is present around 2 µm deep into the Si. For the SiO_2 TRIM simulations, in Figure 2.15a, the most collisions occur at around 3 µm deep. This also coincides with the results of the ion range prediction of 3.38 µm in Figure 2.15c. The most energy loss of the source ion occurs around 1.5 µm deep into SiO_2.

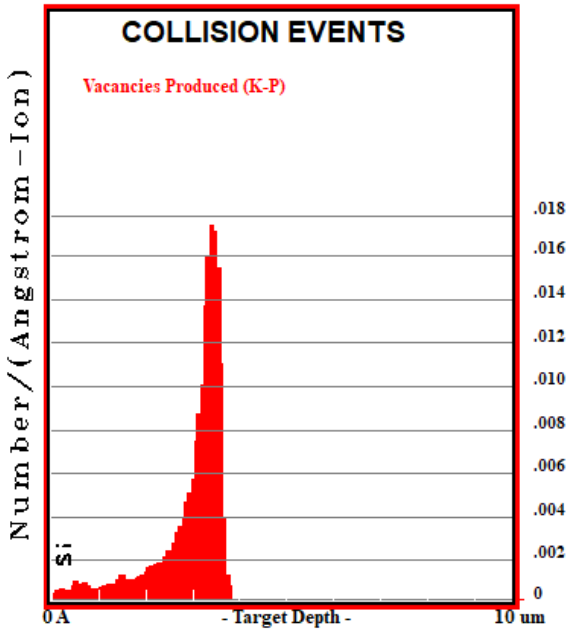

(a) Collisions

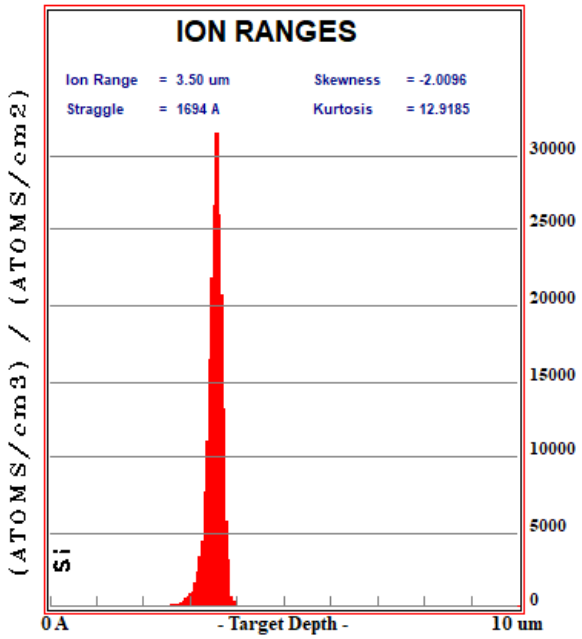

(b) Ion Ranges

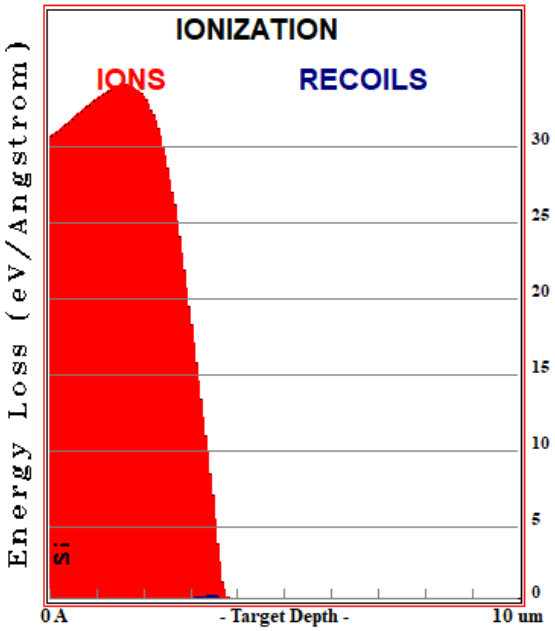

(c) Ionization

Figure 2.14: TRIM alpha particle radiation (1 MeV) simulation with Si as the target.

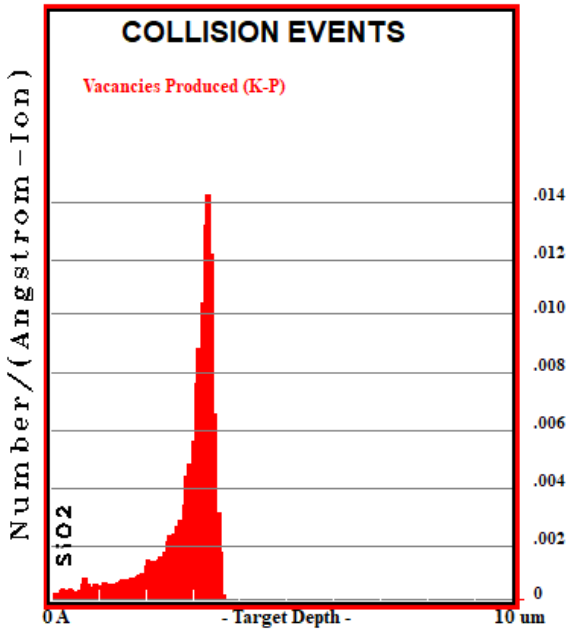

(a) Collisions

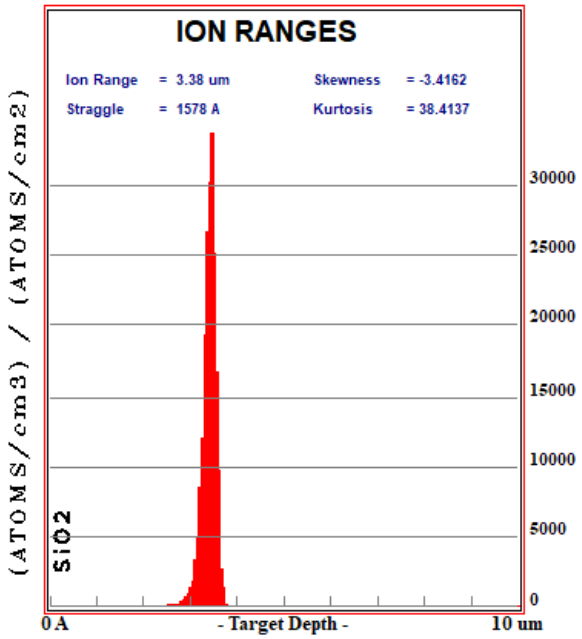

(b) Ion Ranges

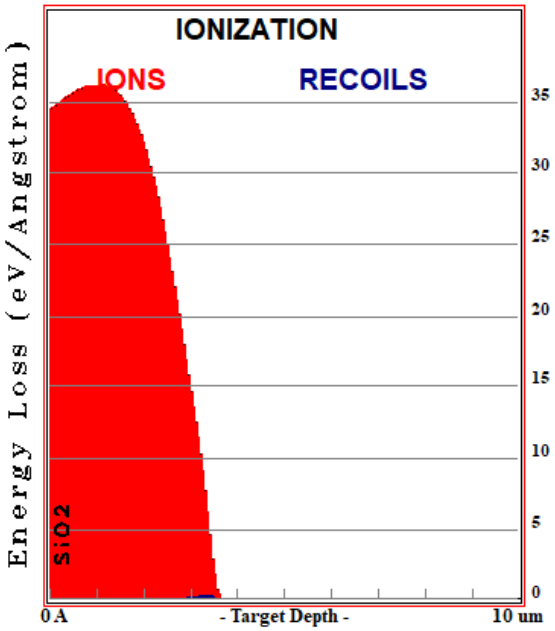

(c) Ionization

Figure 2.15: TRIM alpha particle radiation (1 MeV) simulation with SiO_2 as the target.

Chapter 3

Radiation Analysis and Modeling

3.1 Radiation Effects and Analysis on SiPh Devices

SiPh devices in PICs face various challenges as they gain popularity due to their superior performance compared to their electronic counterparts. Radiation effects have become a significant topic as these devices are introduced in radiation-intensive environments, such as space, as discussed in Chapter 1.

In [18], the requirements for NASA space missions are discussed. High radiation tolerance, greater than 100 krad (Si) TID dose, is needed for long mission durations that may have numerous SEE and DDD events. Such missions may include deploying spacecraft to Europa and being in a geostationary transfer orbit. Moderate radiation tolerance of 10-100 krad (Si) would be suitable for medium duration missions that may still exhibit intense SEE events but moderate DDD events. Missions like these include spacecraft in high and low Earth orbit. Low radiation tolerance of less than 10 krad (Si) would be suitable for short mission durations that experience moderate SEE and minimal DDD events. Such low radiation-tolerant devices may be suitable for the Hubble Space Telescope. The road map for radiation-tolerant devices in [18] includes simulation tools, radiation environment models, on-orbit experiments and validation, and design tools.

Radiation effects on these devices must be studied, and mitigation strategies such as radiation-hard designs must be implemented into SiPh devices. The various radiation effects on SiPh devices are shown in Table 3.1. Waveguides are vulnerable to both TID and DDD, with their effective index being modified. Consequently, modulators are vulnerable to TID effects, lowering their modulation efficiency. Modulation efficiency is crucial to the performance of modulators such as MRMs, and such vulnerabilities to radiation must be mitigated.

Prior work on SOI waveguides has shown some robustness to TID. In [19] several waveguide designs with varying widths for strip and ridge waveguides were exposed to 100 krad (Si) gamma

Table 3.1: Radiation Effects on SiPh devices. Content from [1]

Device	**Laser**	**Modulator**	**Detector**	**Waveguide**
TID	Vulnerable	Vulnerable	Robust	Vulnerable
DDD	Vulnerable	Robust	Robust	Vulnerable
Microscopic defects	Mid-gap state induced non-radiative recombination	Trapped charge induced carrier depletion (pinch-off)	Defect generation	Mid-gap absorption and volume change
Performance Effects	Increased threshold current and decreased slope efficiency	Decreased modulation efficiency	Minimal	Effective index change and increased absorption

radiation. The group index change was negligible, but the propagation loss did increase after the TID, but decreased to mostly pre-irradiation levels after heat treatment. To investigate this further, a 3 µm wide ridge waveguide was irradiated incrementally until 1 Mrad (Si) TID was achieved. Then a thermal annealing of 200 degrees Celsius on a hot place under normal atmospheric conditions for two hours was performed, which resulted in a reduction of the propagation loss from 1 dB/cm to around 0.7 dB/cm. Furthermore, radiation hardness strongly depends on whether a device is passivated or unpassivated. Passivation for a SiPh device includes a layer above the devices themselves, such as SiO_2 cladding. Unpassivated devices are exposed to the surrounding air. In [8], unpassivated MRRs were exposed to 145 krad (SiO_2) TID and 870 krad (SiO_2) TID of 10 keV X-ray radiation exhibiting 0.17 nm blue-shift and a 0.36 nm blue-shift in the resonant wavelength, respectively. The unpassivated MRRs were also exposed to a 147 krad (SiO_2) TID of 662 keV gamma radiation, resulting in a 0.4 nm blue-shift in the resonant wavelength. When the MRR devices were passivated and exposed to the 145 krad (SiO_2) of 10 keV X-rays and 147 krad (SiO_2) of 662 keV gamma rays, they exhibited no change in the resonant wavelength. These findings are further supported by [20], where a passivated MRR experienced an absorbed dose of 15 Mrad TID of gamma radiation and showed minimal shifts in the optical spectrum, demonstrating robustness.

However, in active devices such as MRMs and MZMs, the waveguide has the structure of a p-n junction (see Figure 2.11) which exhibits more vulnerability to TID effects. In [21], MZMs

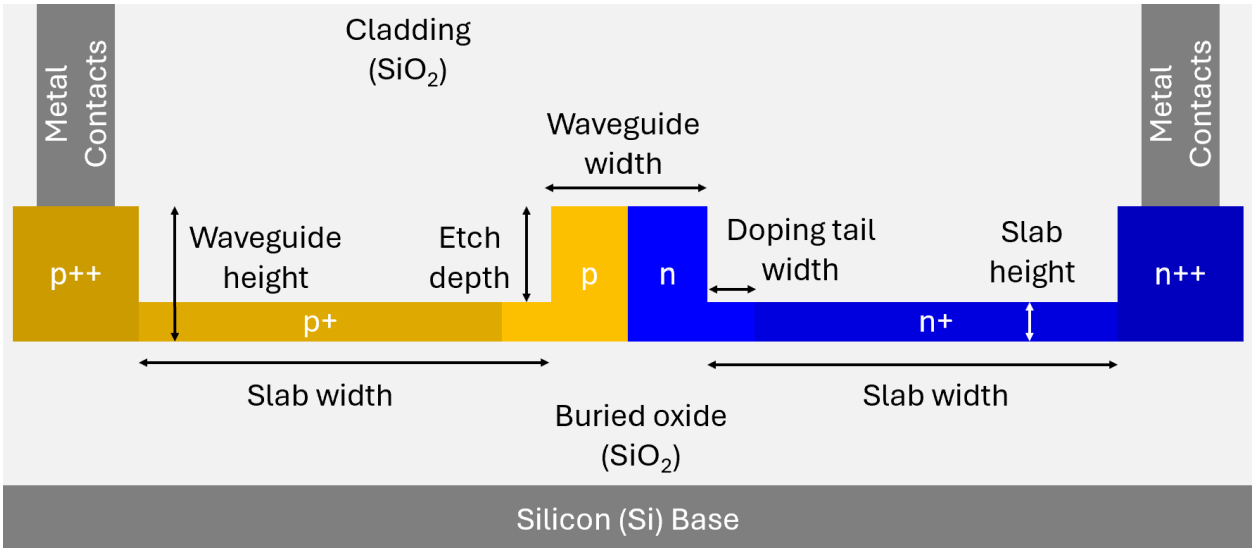

Figure 3.1: Waveguide p-n cross-section implemented on an SOI wafer with all necessary structures present, including metal contacts and regions of varying doping levels. Crucial waveguide dimensions are marked with dark arrows.

experienced TID levels similar to the most extreme cases observed at the High-Luminosity LHC. It was observed that nonionizing radiation did not significantly affect the modulation efficiency of the MZMs; however, the MZMs were sensitive to TID, with essentially no modulation occurring at a MGy of TID. This is further demonstrated in [3] where MZMs exhibited phase shift degradations at high TID levels. Different design parameters were used to explore and identify radiation-hard designs. The parameters included doping tail widths, doping levels, and the etch depth (see Figure 3.1).

MZMs with a deep etch degraded at a lower TID dose than those with a shallow etch, regardless of doping level or doping tail width. A deep etch corresponds with a thin slab, while a shallow etch corresponds with a thick slab. MZMs with twice the nominal doping and having a shallow etch did not experience degradation within the TID limits of the experiment. When the MZMs were irradiated under a reverse bias, their performance degraded at earlier TID levels. The higher the bias voltage during irradiation, the lower the TID dose needed for steep degradation to occur. Lastly, when the MZMs were irradiated at -30 degrees Celsius, there was no degradation present. The steep degradation of the MZMs was explored in [3] with TCAD simulations in Synopsis

Sentaurus. The deep etch nominally doped waveguide p-n junction was simulated before radiation and after 250 kGy of radiation, shown in Figure 3.2.

After radiation, the p-n junction exhibited a pinch-off region where the holes in the waveguide core are separated by defects at the Si/SiO_2 interface and trapped holes in the SiO_2 from the p region of the slab. When a reverse bias is applied, those holes in the core waveguide can no longer be depleted, forming a pinch-off region. MZMs with a shallow etch had a thicker slab, which aided in reducing the effects of these defects, and the holes could still be depleted at higher TID levels. MZMs with higher nominal doping also experienced the same benefits due to the ability to overcome these defects at higher TID levels.

In [2], both MZMs and MRMs were tested for radiation hardness. Two MZMs with the same geometry but with different doping levels exhibited different radiation tolerances. The MZM with the higher doping level in the slab region of the ridge waveguide reached a higher TID before the degradation of modulation efficiency occurred. This radiation-hard MZM was tested against a third MZM with the same slab doping but with a shorter doping tail width. The MZM with the shorter doping tail width had an even more radiation-hard design with much less degradation of the modulation efficiency at very high TID levels compared to the other design. The authors in [2] attribute the increased radiation hardness from a decreased doping tail width to a smaller possible pinch-off region. The possible pinch-off region is smaller when the doping tail width is decreased. Also, the p-region of the slab can compensate for the holes in the waveguide core more easily if the doping tail width is minimized. The same is true for a higher doping level in the slab region, where the holes in the waveguide can be compensated for and the possibility of pinch-off is reduced.

The literature presented in this section highlights the crucial role of SiPh device design in their radiation hardness and the complexity involved in developing radiation-hard devices.

3.2 Radiation Aware Modeling

The current state of the art in radiation modeling in active SiPh devices is found in [22]. The authors used a theoretical model for fixed charge and interface trap development from irradiation.

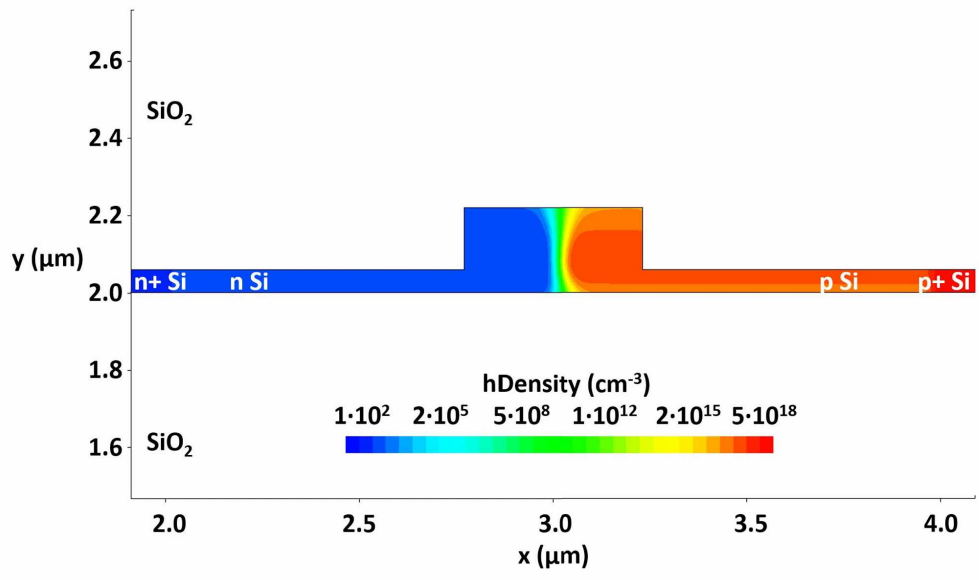

(a) MZM

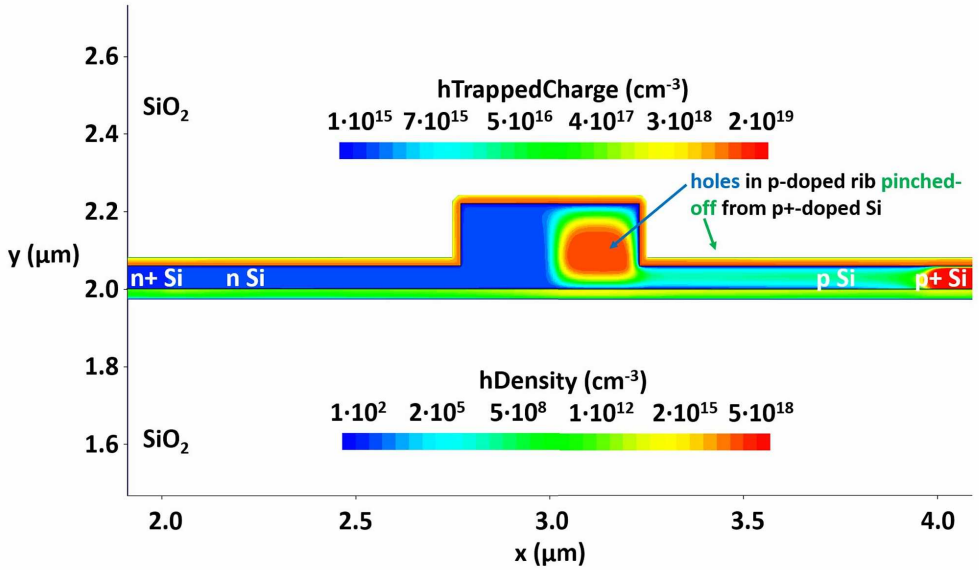

(b) MRM

Figure 3.2: (a) Waveguide before radiation. (b) Free hole density in the phase shifter with trapped hole density in the SiO_2 overlaid after 250 kGy for a deep etched MZM. The holes in the phase shifter are pinched off from the slab region. Plot reproduced from [3] (Licensed under CC BY 4.0).

The structure of the device is defined, then passed through an electromagnetic wave solver along with a device solver, and finally, a change in the loss and effective index of the device is found. The damage from accumulated irradiation is inserted at every time step. Therefore, the device's effective index and loss are calculated at every time step with increasing TID. This simulation found reasonable accuracy compared to experimental results.

The novel contribution of this thesis is the development of RADPIC, a radiation-aware design-space exploration and simulation framework to study the impacts of TID on SiPh devices based on the SOI platform. This proposed platform follows a bottom-up approach, by first finding the material refractive index change and interface traps generation from the effects of a TID dose, then the electrical and optical properties of the SiPh devices are gathered through electro-optic simulations.

RADPIC is built upon analytical models that capture the impact of radiation at the material level and leverages Ansys Lumerical tools [23] for electro-optic simulations. The core structure of RADPIC is inspired by a simulation framework for an MRM from Ansys [24]. The flow of the RADPIC framework can be visualized in Figure 3.3 where each step is briefly defined and the outputs described.

Given an input TID dose, the change in the material refractive index and the interface trap charge density are calculated. Then these modified materials are inserted into a predefined 3D structure of a SiPh device in the finite-difference time-domain (FDTD) simulation, a 3D electromagnetic solver. These modified materials are also inserted into a predefined 2D or 3D structure in the finite difference eigenmode (FDE) simulation called MODE, a solver that calculates the spatial profile and frequency dependence of modes. The calculated interface trap charge density is inserted into the electrical simulation, called CHARGE, which outputs a spatial charge distribution mesh for an applied bias voltage. This mesh is inserted back into the FDE (MODE) simulation to find the effect of radiation on the p-n junction at varying applied voltages on the modal properties inside the SiPh device under simulation. The outputs from these simulations are all gathered into the circuit-level simulation, called INTERCONNECT, for device-level analysis.

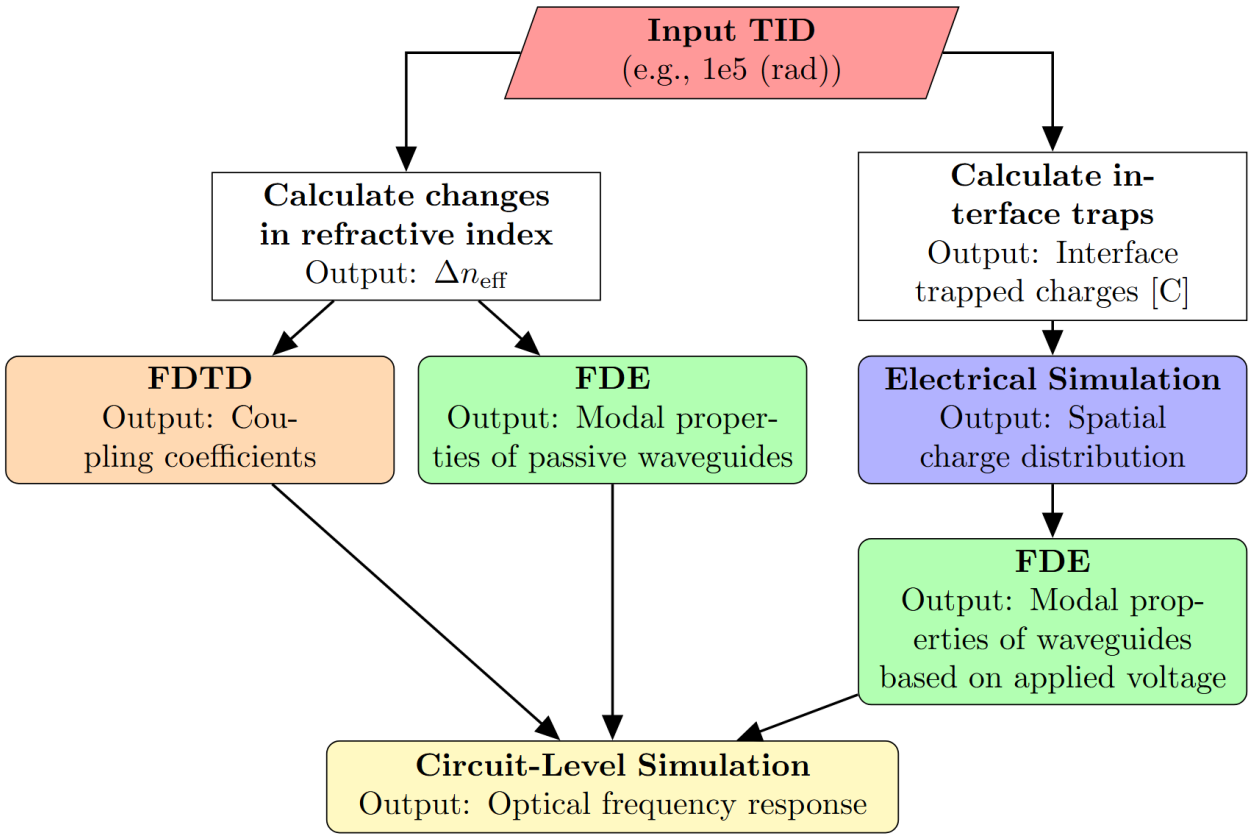

Figure 3.3: The RADPIC framework starts with radiation effects calculated at the material level, then inserted into various solvers, which ultimately allow for circuit-level simulations, allowing for device-level analysis.

To obtain the changes in the refractive index for Si and SiO_2, as well as the interface traps generated at the Si/SiO_2 interface, we first use analytical models that take the radiation dose as input. Note that the generation and effects of electrons were not included in our calculations because, as previously discussed, electrons quickly escape upon generation. To calculate the changes in the refractive index, (2.11) can be modified to

$$\Delta n = \frac{-e^2\lambda^2}{8\pi^2 c^2 \epsilon_0 n}[\frac{\Delta N_h}{m^*_{ch}}]. \tag{3.1}$$

Here, ΔN_h comes from (2.15). The changes in the refractive index at a given input radiation dose are combined with the nominal refractive index of each material to calculate the new refractive index values for Si and SiO_2.

The interface trap charge density can be calculated using (2.15). The values for g_0 for Si and SiO_2 can be retrieved from [25]. A scale factor was introduced for ΔN_h in both (2.15) and (3.1) as these equations were generating extremely large shifts in the refractive index and interface charge density. These large values, when used in simulation, would break down convergence in the simulations (a value of 10^4 worked well to address these challenges).

Since RADPIC inserts radiation effects at the material level with equations (3.1) and (2.15), it lends itself to being highly configurable. The active SiPh design of interest can be prepared in the individual simulations, and RADPIC will obtain the device performance at each TID level of interest, resulting in a comprehensive analysis of device performance under radiation effects. To more fully describe the working principle of RADPIC, a case study is presented in the next chapter.

Chapter 4

Ring Modulator Case Study

To illustrate a practical implementation of RADPIC, a case study is presented where an MRM is simulated based on a previous study, [2], and the results of the RADPIC simulation framework are compared with the experimental results of this study. As explained in Chapter 1, RADPIC is built on the backbone of an Ansys MRM simulation framework [24]; therefore, it is fitting that this case study involves an MRM. The following sections will discuss each step of the RADPIC simulation framework.

4.1 Applying Analytical Models

Ansys Lumerical simulation tools, FDTD and MODE, contain predefined properties for various materials, including Si and SiO_2. In order to implement radiation effects, (3.1), in these simulations, custom Si and SiO_2 materials were required. The default data for Si and SiO_2 refractive index were downloaded from the *Material Explorer* within Ansys Lumerical tools, such as FDTD. The data included the refractive index for the material at all wavelengths of interest. From this, (3.1) was used to alter the refractive index based on the input TID dose. The output from this equation is part of the input for the new custom Si and SiO_2 materials that will be used for the FDTD and FDE (MODE) simulations. These materials are automatically inserted within the RADPIC framework scripts.

To include radiation effects in the electrical simulation, in CHARGE, the trapped charge density at the Si/SiO_2 interface must be calculated. This can be done using (2.15). The output of this equation was scaled down with a scaling factor because not all of the charges generated in (2.15) are directly located at the interface. The scaling factor is a parameter that can be set in the scripts of RADPIC.

4.2 Electromagnetic Simulation

Electromagnetic simulations are performed with the Ansys FDTD tool. The purpose of the FDTD simulation, with respect to the MRM, is to obtain the coupling coefficients from the input waveguide to the ring. That is, how much of the light from the input waveguide couples into the ring at each frequency. The MRM structure is shown in Figure 4.2 and Figure 4.1.

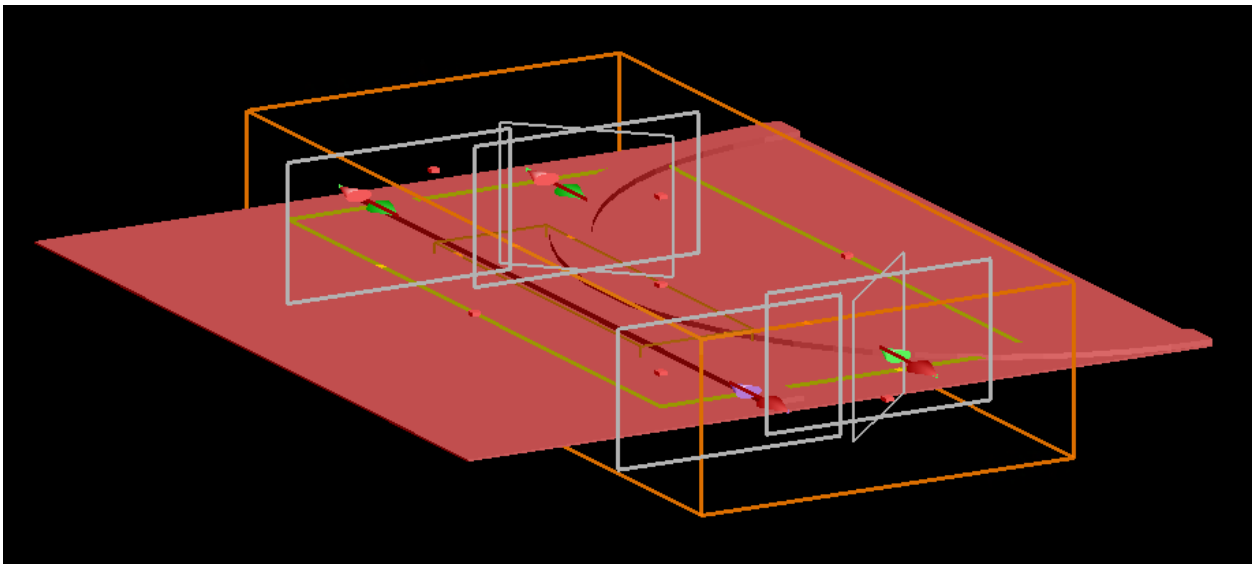

Figure 4.1: FDTD simulation 3D view. The objects made from Si are shown in red: the input waveguide, the bent waveguide (the MRM ring), and the slab. SiO_2 is not visible; it is set as a background material. The simulation region is enclosed in the orange 3D border. The purple arrow (input port) is where light is injected into the simulation, with the other ports collecting data (gray screens).

It consists of a straight waveguide in proximity to a bent waveguide (which represents the ring). In practice, the bent waveguide would loop fully, creating a ring shape; however, for simulation purposes, only half the ring is necessary to characterize the coupling of the light from the input waveguide to the ring. Both of these waveguides are on top of a base layer of Si, meaning that these waveguides are of the ridge type. SiO_2 is the background material used for the simulation, and it is not visible in this simulation. The simulation includes 4 ports shown in pairs of arrows. These arrows represent the mode or wave propagation within the waveguide. The top left port of Figure 4.2 is where the light is injected into the device, and the other ports monitor and collect the data on the propagation of light through them. As the light travels from the top left port and

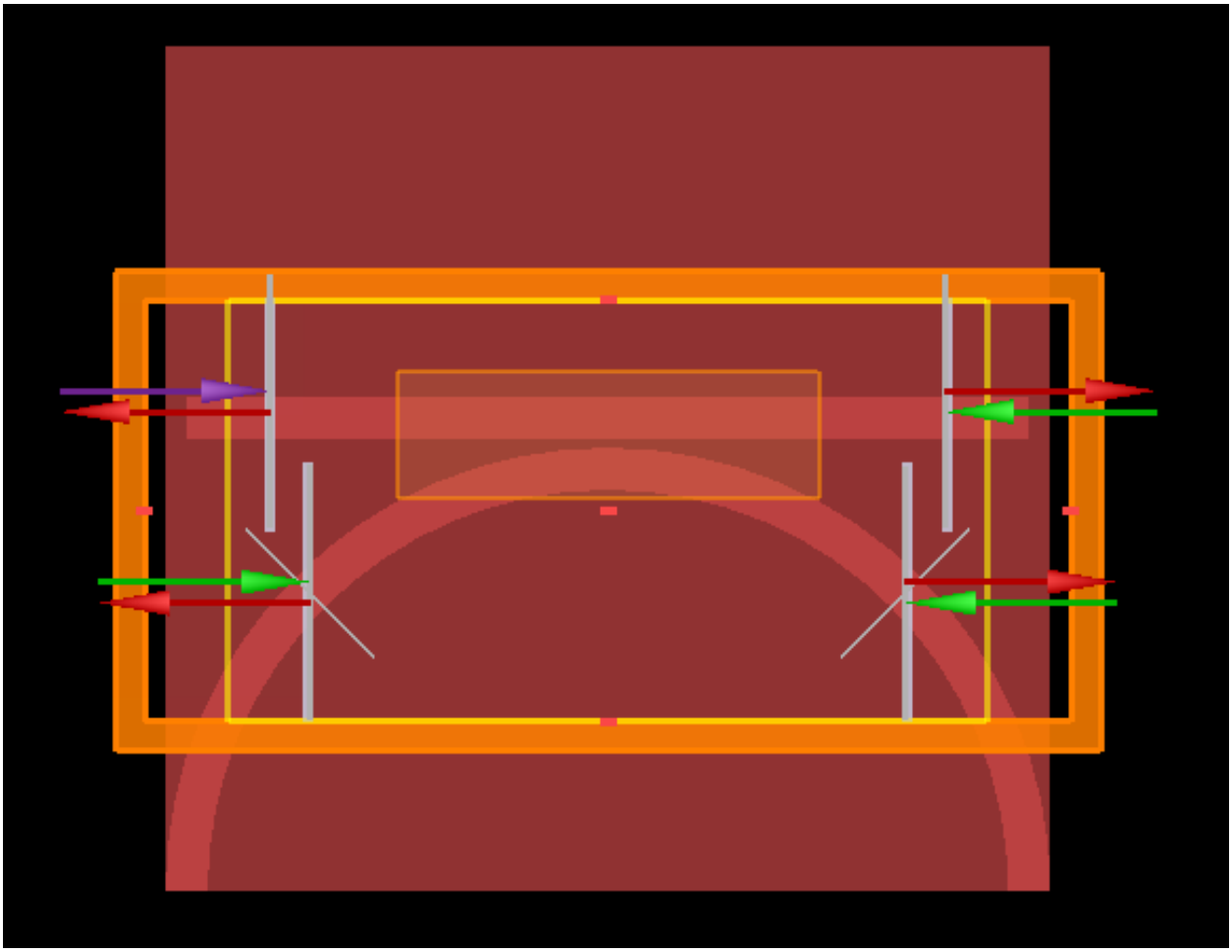

Figure 4.2: FDTD 2D simulation view with Si structures shown in red, SiO_2 is not visible as it is the background material, the simulation boundary is shown in orange, and the ports with arrows and gray screens.

couples into the ring, it will pass through the bottom right port. Therefore, the bottom right port, on the bent waveguide, is used to collect the coupling coefficients of the device. The path of the light within the device can be visualized in Figure 4.3, which further illustrates the role of the bottom right port in the collection of the coupling coefficients. Once the text file for the coupling coefficients is complete, the simulation framework can move on to the next task.

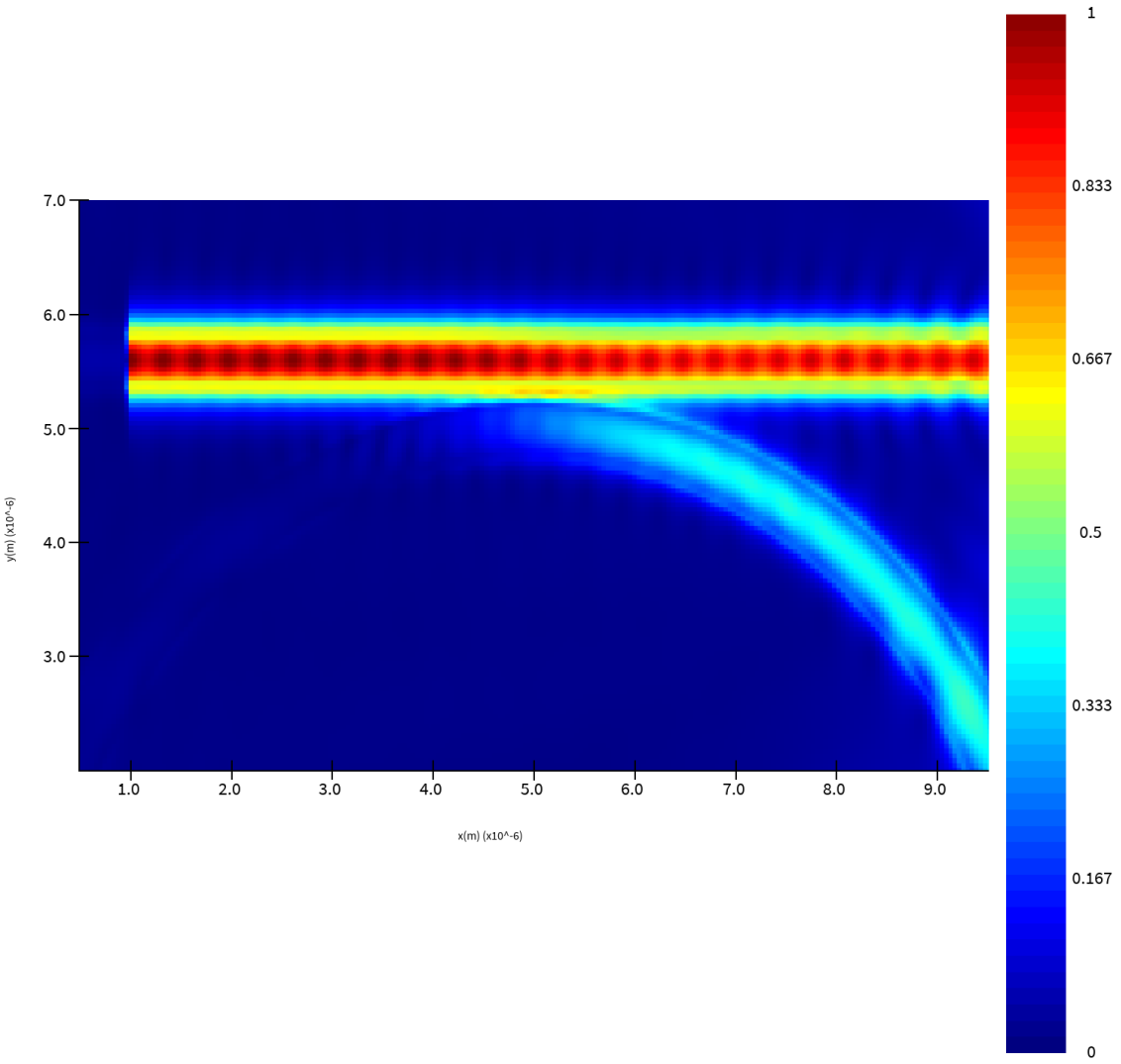

Figure 4.3: Coupling of light from the input waveguide to the ring. The electric field magnitude is shown in color with the color bar for reference.

4.3 Electrical Simulation

Electrical simulations can be performed using the CHARGE tool from Ansys. This simulation requires only a cross-section of the active components of the SiPh device. In the MRM, the active structure p-n junction that exists as part of the waveguide structure, for the majority of the ring. Since the waveguide within the ring device is identical throughout the ring, only one cross-section of it is needed. In Figure 4.4, the ridge waveguide is present in the center, shown in purple, with

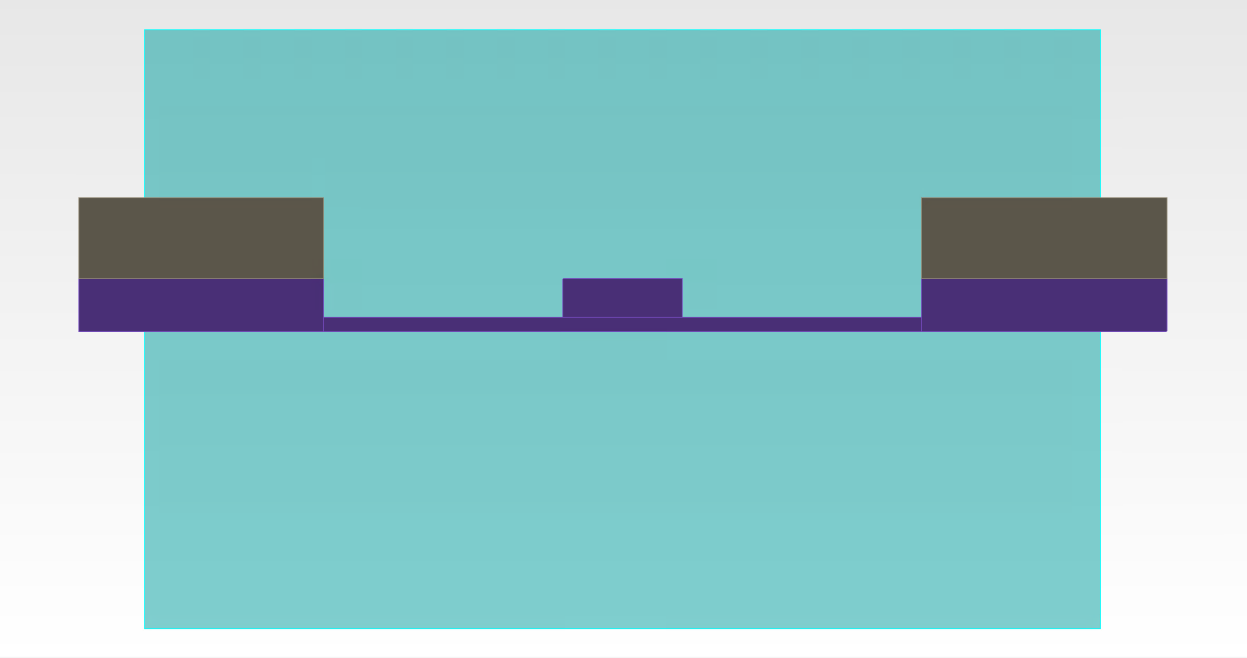

Figure 4.4: CHARGE simulation overview. The cross-section of the Si waveguide is shown in purple, SiO_2 is shown in light blue, and the electric contacts are shown in dark gray.

the slab extending outwards away from it until it enlarges to reach the metal contacts shown in gray. These metal contacts are where the bias is applied to the p-n junction within the waveguide. The background material is SiO_2 shown in light blue. The boundary between the Si and SiO_2 is where the interface trap charges are located. A boundary condition is created to include these traps in the overall simulation, and it is illustrated in Figure 4.5. The black line that outlines the waveguide structure and slab is where the trap charge density, calculated at the start of the framework, is inserted. The highlighted green section in Figure 4.6 is useful to visualize the doping regions

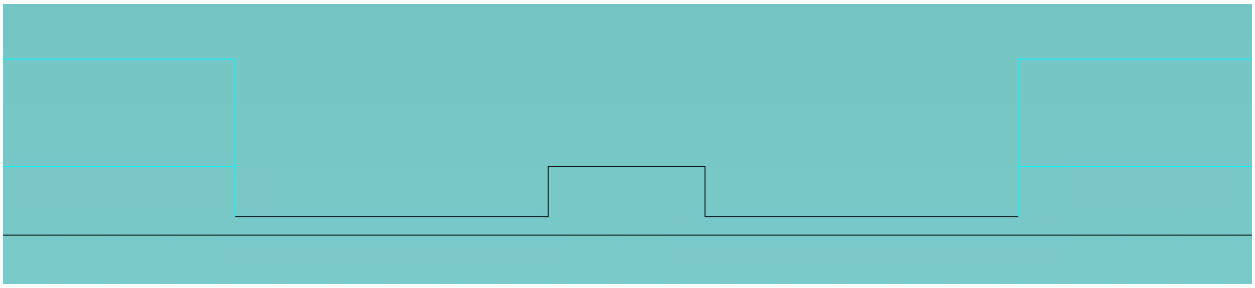

Figure 4.5: Si/SiO_2 trapped charge interface boundary shown with the highlighted black lines.

of the p-n junction within the waveguide, slab, and Si near the metal contacts. The regions are symmetrical from the middle of the waveguide. To the left is the n-doped region, and to the right is the p-doped region. The doping here follows the structure laid out in Figure 3.1 with the waveguide along with the doping tail and the slab having unique doping concentrations. Visualization

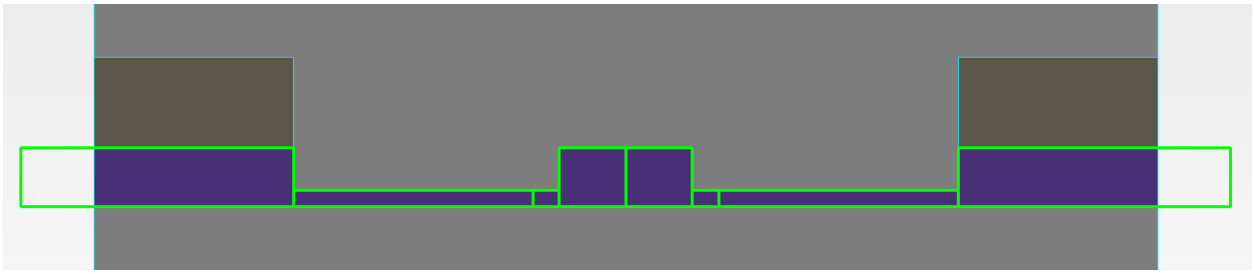

Figure 4.6: The various doping regions within the CHARGE simulation are shown with green borders.

of the doping concentrations is shown in Figure 4.7 where the hole concentration is illustrated by various colors representing concentration. The left side of the waveguide and related structures is dark blue due to the absence of holes in the n-doped region. The right side of the waveguide and related structures have varying amounts of doping concentration following the same pattern as Figure 3.1. When the CHARGE simulation runs, it simulates the charge carrier concentration within the waveguide at various applied voltages and saves data on the spatial distribution of these charges, creating the charge distribution mesh. The radiation dose applied to the CHARGE simulation material interface boundary will also have an effect on the mesh, which is how the electrical simulation encapsulates the radiation effects on a p-n junction within a SiPh device. This data can later be used in optical simulations to include the effects of the p-n junction on mode propagation.

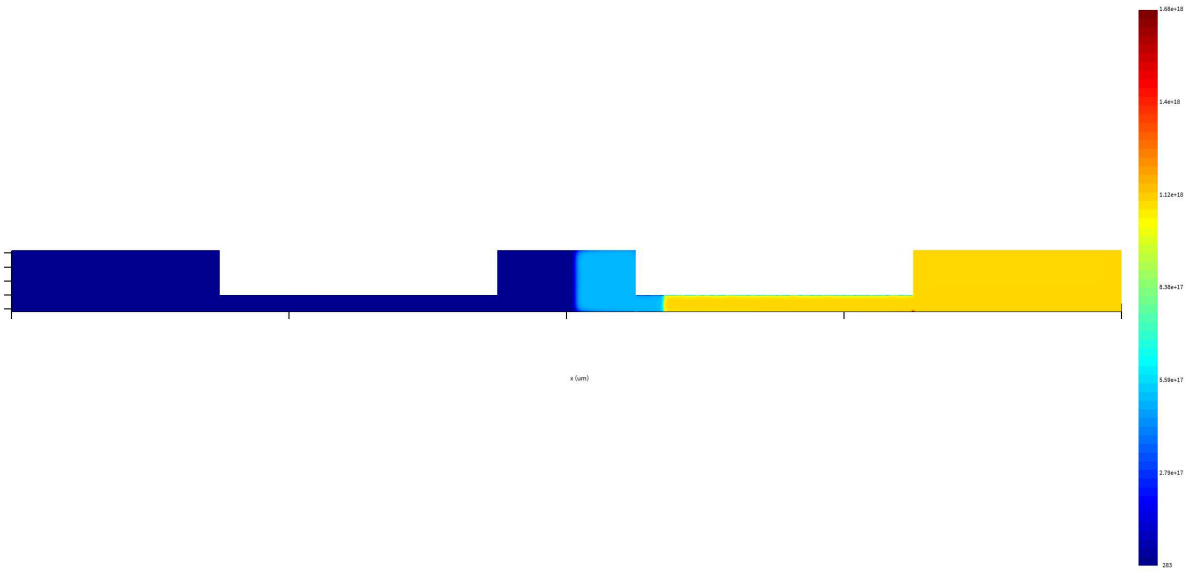

Figure 4.7: Nominal, no radiation effects, hole concentration in the CHARGE. Hole concentration is shown with a color gradient described by the color bar.

4.4 Modal Properties Simulation

To obtain the modal properties of a photonic waveguide, the MODE tool is used. The primary function of the MODE simulations includes obtaining the frequency-dependent effective index for the passive (undoped) and active (doped with applied bias) portions of the MRM ring. The input waveguide is passive, with no doping. The ring has a certain percentage of the bent waveguide passive, with the remaining section being active. The percentage of the ring that is doped is a design choice made carefully based on the application of the MRM. In Figure 4.8 and Figure 4.9, the simulation is visualized. The waveguide and slab are shown in red. The purple mesh overlaid on the waveguide is the spatial charge distribution obtained from the CHARGE simulation. When simulating the passive waveguide and the passive bent waveguide, this mesh is disabled. It is enabled for the active bent waveguide simulation only. Although the structures in the simulation can be 3D, the simulation itself is a 2D cross-section at the center of the structure, in the same location as the charge distribution mesh. Since the simulation runs on a 2D cross-section of the waveguide, there is no innate sense of a bend occurring, and it is a specific feature that must be

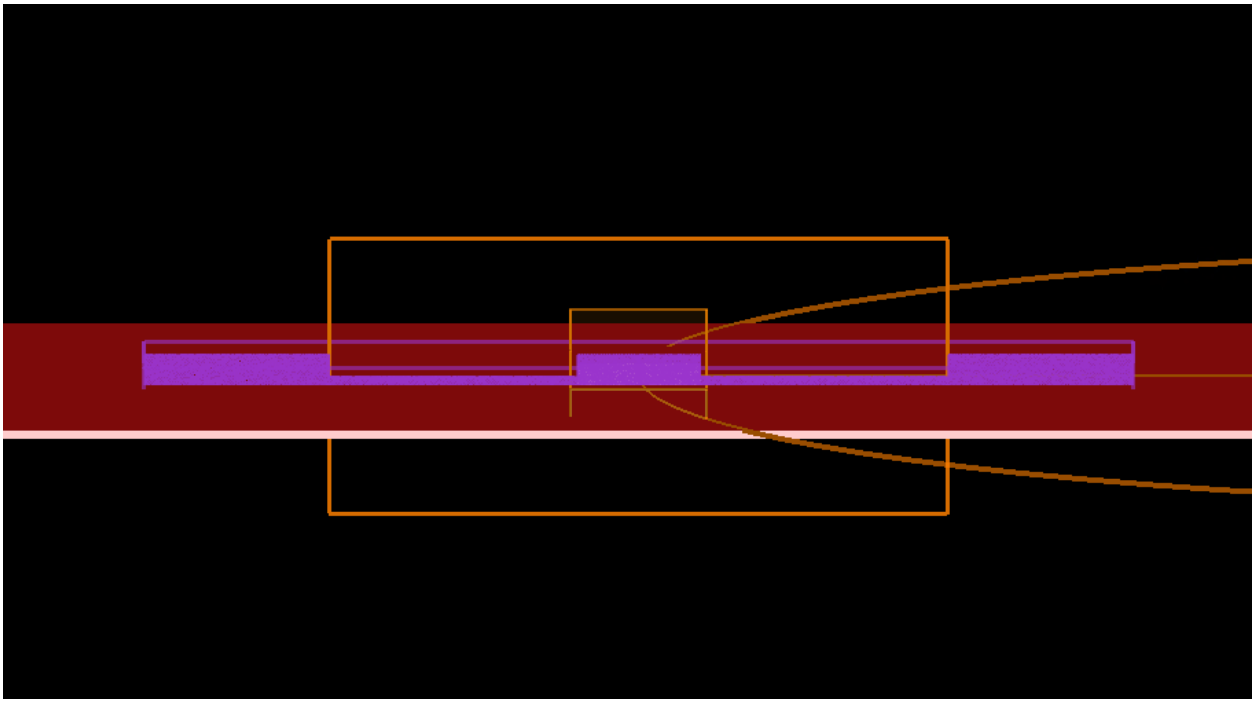

Figure 4.8: MODE 3D view. The Si structures are shown in red with the spatial charge distribution mesh (from CHARGE) overlaid on top in purple. When the bend setting is enabled, as shown here, an orange circle is visible in the simulation representing a continuously bent waveguide. SiO_2 is not visible here since it is set as a background material.

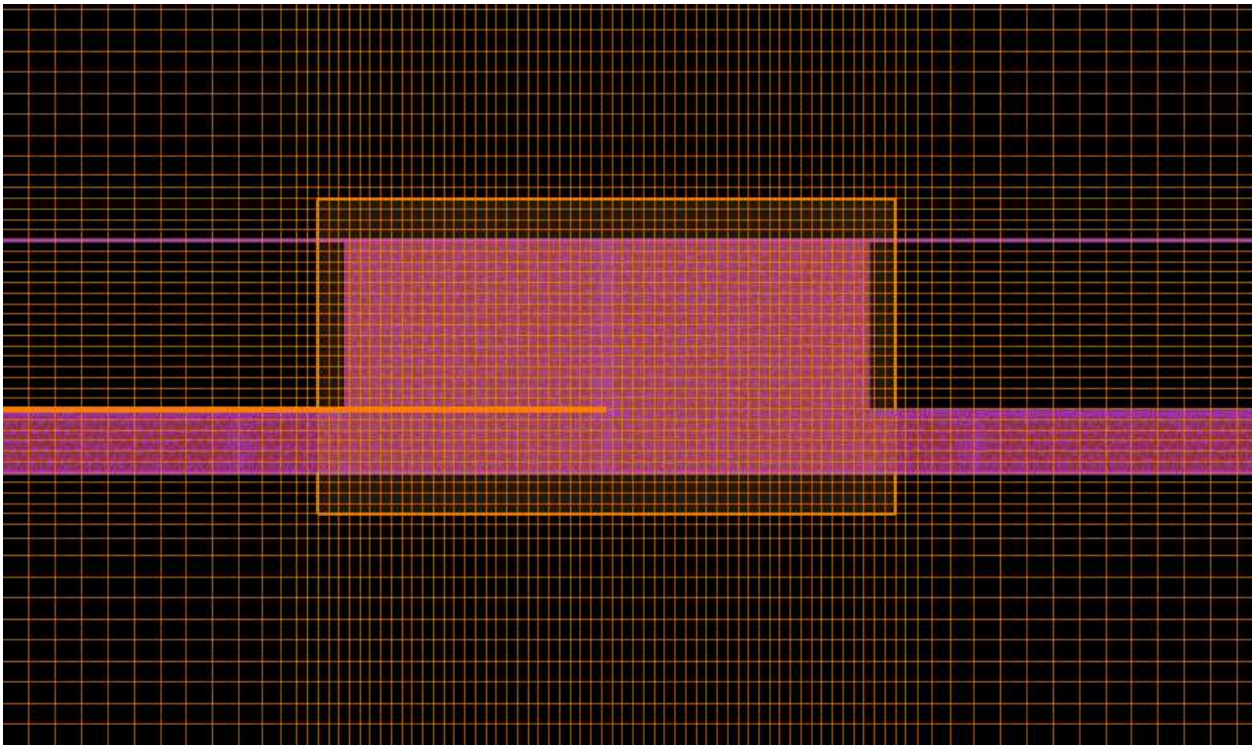

Figure 4.9: MODE 2D view with a close-up of the Si waveguide with the spatial charge distribution mesh visible in purple. A small orange mesh region is visible too, which is only used for increased solver calculations in the region.

enabled. Therefore, the simulation must be run separately for the passive straight, passive bent, and active bent waveguides. After all three of these simulations are done, the effective index and related frequency-dependent data are saved in three separate Lumerical data files. The final step of the MODE simulation includes running a voltage sweep script provided by Ansys in [24]. This script sweeps through applied voltages in the active bent waveguide to calculate the change in the effective index from each applied reverse bias from -1 V to -10 V. This data, saved into a text file, will be used in conjunction with the Lumerical data files in the final step, circuit-level analysis.

4.5 Circuit-Level Simulation

Circuit-level simulations can be performed in INTERCONNECT, where device performance can be analyzed. This simulation brings together all of the files obtained from the previous simulations, including: coupling coefficients text file, passive/active bent waveguide and passive straight waveguide Lumerical data files, and change in effective index per applied bias text file. The MRM, shown in Figure 4.10, is recreated with circuit components such as directional couplers, waveguides, modulators, and a voltage source. All of the waveguides outside the ring are loaded with the passive straight waveguide data. The directional couplers are loaded with the coupling coefficients, and the ring contains two waveguides, where one is loaded with the passive bent waveguide data and the other is loaded with the active bent waveguide data at no applied voltage. A modulation component is inserted in the ring connection, which modulates the effective index based on the applied voltage from the voltage source. The extent to which the effective index is modulated is governed by the change in the effective index file loaded into the modulator. To analyze the behavior of the MRM, an optical network analyzer (ONA) is connected to the MRM, and it collects the optical transmission response from the through port and drop port. In many cases, the through port is sufficient for MRM performance analysis. When the simulation is run, the ONA analyzes the response of the MRM over many input light wavelengths. The simulation must be run once for every applied voltage, and the transmission data of the MRM is saved for each simulation run. When all simulation runs are finished, the data can be plotted to visualize the impacts of radiation on

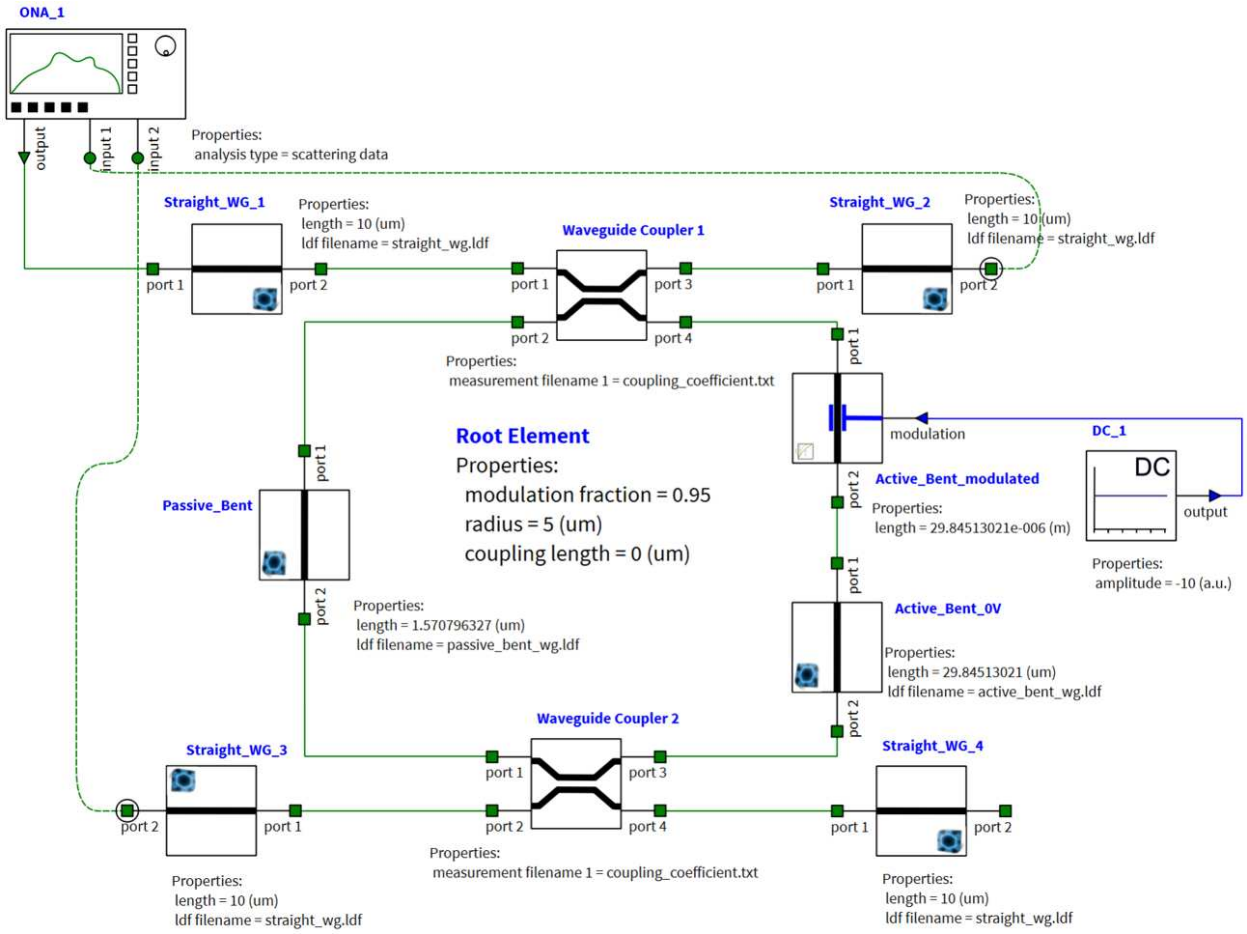

Figure 4.10: INTERCONNECT overview. The MRM is composed of fundamental components that are loaded with data collected from FDTD, CHARGE, and MODE to accurately represent the MRM design of interest.

transmission at different applied voltages. Taking this further, the shift in the peak of the transmission dip from one applied voltage to the next can be used to calculate the modulation efficiency. Running the full RADPIC framework through different TID levels can allow for comparing the impacts of radiation damage on the modulation efficiency of an MRM. Scripting is implemented in RADPIC to run through different TID levels automatically.

4.6 Validation of RADPIC

To validate RADPIC, we compare the simulation results from RADPIC with the MRM experimental data from [2]. In this work, there were three different MRM designs tested. Each design had the same physical dimensions, but the doping concentration in the p-n and p+-n+ regions was varied as described in Table 4.1. The table shows the relative doping concentration to the base doping concentration level of $10^{17}\,\mathrm{cm}^{-3}$. The MRM designs shared the same ring radius of 5 µm, 100 nm gap, a waveguide core width of 500 nm, a doping tail width of 100 nm, a SOI thickness of 220 nm, an etch depth of 160 nm, and slab length of 1 µm. Note that not all the design parameters were available in [2], so some parameters were estimated to the best of our knowledge, such as SiO_2 thickness. All of these geometrical features are illustrated in Figure 3.1. In [2], the main per-

Table 4.1: MRM relative doping concentration for each design in [2]. These designs were used for RADPIC validation. The regions referred to in this table are illustrated in Figure 3.1

MRM Design	Relative Doping Concentration	
	p/n	p+/n+
b	5x	11x
b'	1x	50x
b"	10x	50x

formance metric was the normalized modulation efficiency of the MRM to determine the radiation hardness of each MRM design. The modulation efficiency measured the shift of the transmission dip from 0 V to 1 V reverse bias. The MRM designs were recreated within each of the Ansys tools

previously described. The modulation efficiency was studied among other performance characteristics, including Q-factor, ER, and FSR for all the MRM designs in Table 4.1.

The results for the modulation efficiency are shown in Figure 4.11 with simulation data collected in RADPIC shown in Figure 4.11a and the experimental data from [2] shown in Figure 4.11b. In general, the output of RADPIC is in general agreement with the experimental data from [2]. MRM designs *b* and *b"* follow the trends of the experimental data the closest, while design *b'* initially follows the experimental trend but deviates at the highest TID dose, 10^7 Gy. This demonstrates the ability to simulate radiation-induced damage in MRMs in RADPIC. One of the uniquely important features of RADPIC is the simulation of trapped charges at the Si/SiO_2 interface using a charge boundary condition shown in Figure 4.5. The TID dose applied to the simulation directly affects the concentration of charges placed on this border. However, RADPIC currently does not include a broad range of physical constraints that would be governed by other boundary conditions. This is most likely the reason for design *b'* to deviate from the experimental data at extremely high TID doses, such as 10^7 Gy. This design had the lowest doping concentration in the waveguide core region. This low doping concentration, paired with extremely high TID levels, could easily allow for minor physical effects to take over, which may have allowed for excess charges in the Si/SiO_2 transporting through the p-n region in the CHARGE simulation. This excess amount of charge transport allowed for an overestimated modulation efficiency. Despite this, RADPIC overall effectively captured key physical behaviors of MRMs under radiation-induced damage, as indicated by the strong general agreement between the RADPIC simulation and the experimental results. This can be illustrated by focusing on design *b* and *b"*. For design *b* in RADPIC, the modulation efficiency initially rises from a normalized value of 1 to 1.2 at 10^5 Gy after which it steeply drops to 0 at the highest TID levels. This behavior closely follows the experimental results where design *b* rises roughly linearly from a modulation efficiency of 1 to roughly 1.2 at 10^5 Gy before sharply dropping to 0 right before reaching 10^6 Gy. For *b"* in RADPIC, the modulation efficiency initially stays flat until rising to a modulation efficiency of around 1.1 at 10^6 Gy and remaining at that modulation efficiency for higher TID levels. In the experimental results, *b"*

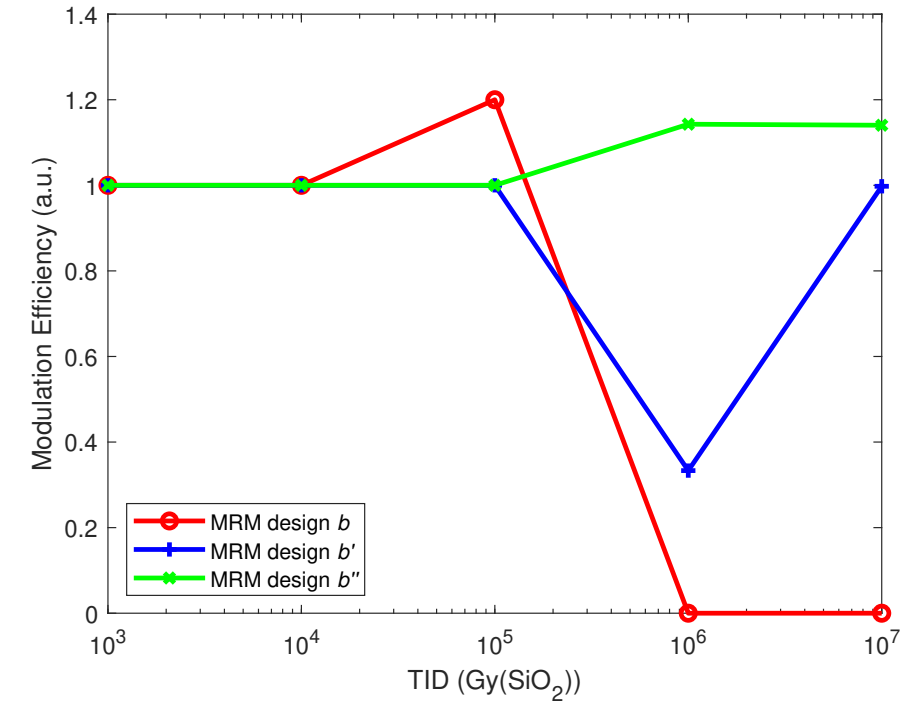

(a)

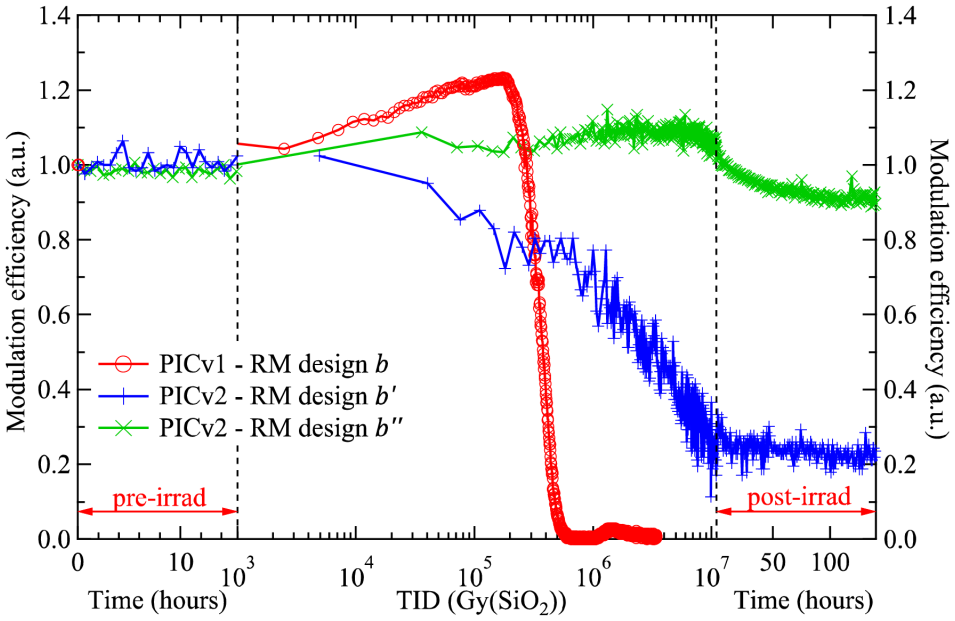

(b)

Figure 4.11: (a) Normalized modulation efficiency simulation in RADPIC for different MRM designs in Table 4.1, plotted for 0 to 1 V. (b) Experimental data reproduced from [2] (Licensed under CC BY 4.0). RM here refers to the same device as MRM. Designs *b* and *b"* closely follow experimental results, while *b'* deviates from the experimental data at the highest TID level.

rises to a modulation efficiency of around 1.1 at 10^6 Gy and stagnates for the remainder of the TID levels. There is one blip in the data where the modulation efficiency jumps to 1.1 after reaching 10^4 Gy that is not seen in the RADPIC simulation results. The sharp drops in modulation efficiency can be attributed to the buildup of the pinch-off region within the p-n junction, where the carriers are no longer able to be depleted, greatly reducing the modulation efficiency. RADPIC accurately reproduces these pinch-off regions, and that contributes to the degradation in modulation efficiency following the trend from the experimental data.

The pinch-off regions developed in RADPIC are shown in Figure 4.12. Here, red conveys a

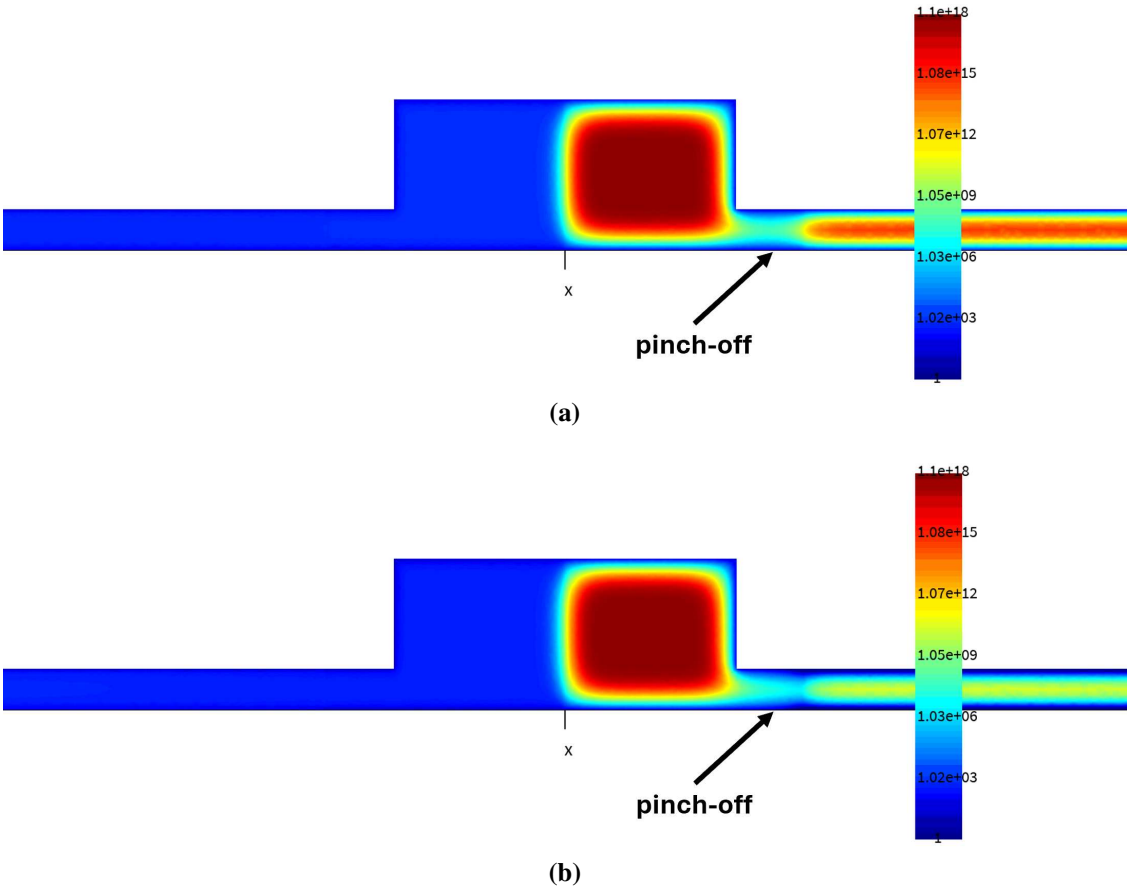

Figure 4.12: Pinch-off occurring at 10^6 Gy (SiO_2) for design *b*. Practically no modulation occurs when 4 V of reverse bias (b) is applied when compared to 0 V (a). The concentration of holes is shown with a color gradient described by the color bar on the right. The main concentration of holes in the waveguide core remains the same across different applied voltages, illustrating the consequences of the pinch-off region.

high concentration of holes and blue shows an absence of holes. In Figure 4.12a, there is no bias

voltage applied, and the holes are present in the waveguide core, the slab, but have a very low concentration in the doping tail region. The holes in the waveguide core are pinched off from the holes in the slab due to the interface trap charges repelling holes, keeping the doping tail region empty of holes. When a 4 V reverse bias is applied, as illustrated in Figure 4.12b, the holes in the waveguide core remain at a similar concentration as when there was no reverse bias applied. However, the 4 V reverse bias did deplete the holes present in the slab of the waveguide structure, showing that the pinch-off region is in fact the reason for the carriers not being able to be depleted from the waveguide core.

4.7 MRM Modulation Efficiency Under More Bias

To expand on the experimental data from [2], the RADPIC simulations included the additional reverse bias voltages as shown in Figure 4.13. The modulation efficiency from 0 V to 1 V has already been compared to the experimental data. The modulation efficiency at higher reverse bias voltages reveals more drastic changes. For design *b*, there was a negligible change in modulation efficiency at higher reverse bias voltages. However, for design *b"*, a rapid degradation at the highest TID level occurs at the 4 V and 10 V reverse bias, which was not observed at the 1 V reverse bias. This is most likely due to a pinch-off region forming. At these higher reverse bias voltages, the charges in the waveguide structure are more depleted, allowing for the interface trap charges to have a stronger impact in the waveguide core region. Lastly, design *b'* unfortunately became even more susceptible to higher TID levels, with the modulation efficiency dropping at 10^5 Gy, where for 1 V reverse bias, the modulation efficiency dropped at 10^6 Gy. This is most likely attributed to the fact that the p-n region is lightly doped, allowing for the interface trap charges to have a greater effect on the region. The continued increase of the modulation efficiency for *b'* at higher TID levels may still be a result of limitations in the physical constraints of the model.

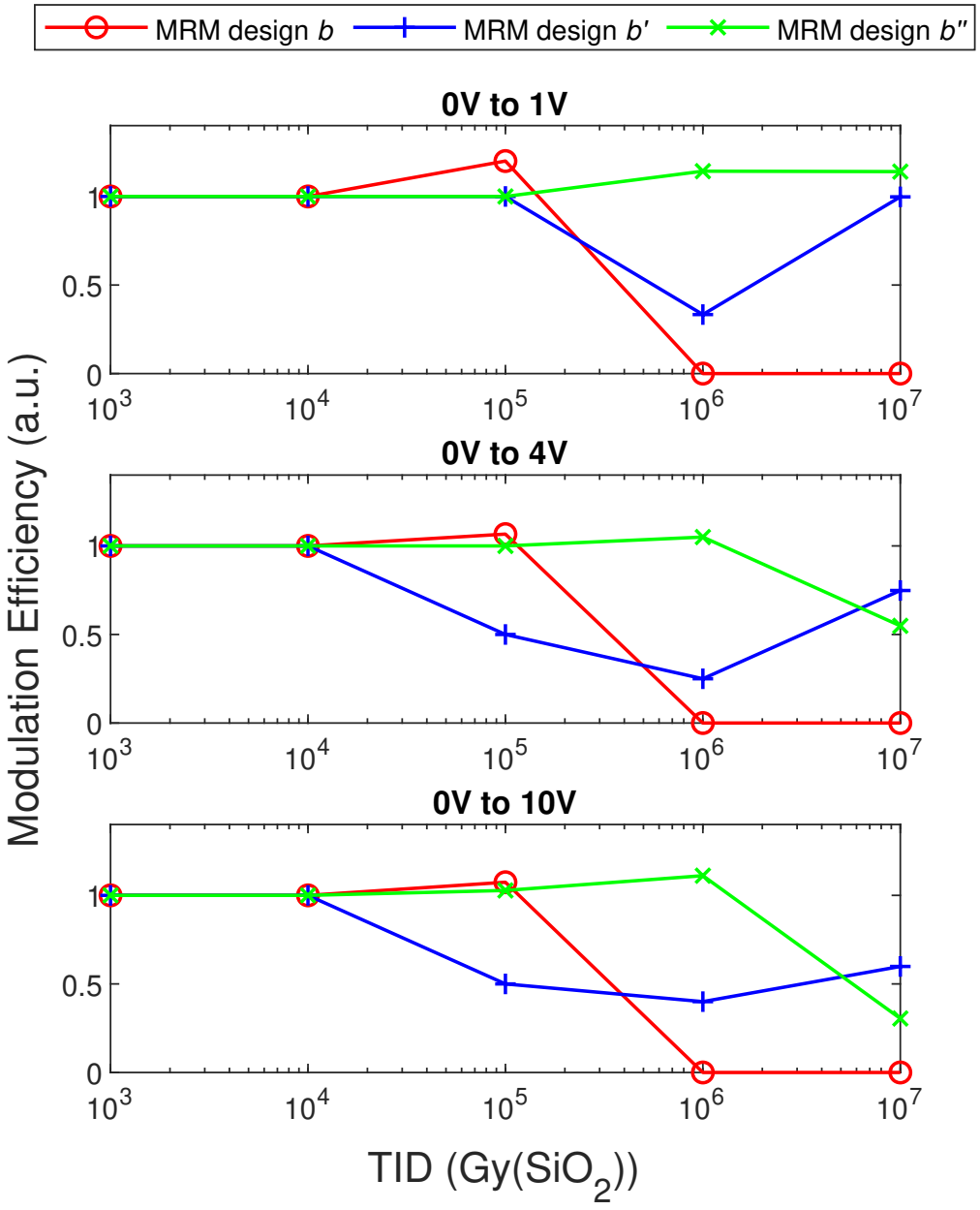

Figure 4.13: Normalized modulation efficiency across different applied reverse biases. Designs *b* and *b"* experience negligible change in radiation hardness, while *b'* shows an increased sensitivity at higher TID levels.

4.8 MRM Performance Under Radiation

The RADPIC simulation captures the optical frequency response for each MRM design at varying radiation doses and reverse bias levels. This allows for analysis of optical responses to extract key properties that are crucial to fully characterize MRM performance. One important property is the Q-factor, which is shown for every design in Figure 4.14. In these plots, the Q-factor decreases with increasing TID levels. Design *b"* experienced the smallest changes in Q-factor consistent with its minimal change in modulation efficiency. Radiation-induced changes in the effective index of the MRM and the increased optical loss due to the presence of more carriers in the waveguide are mainly what contributed to the decline in the Q-factor. More specifically, at higher TID levels, the refractive index of a material decreases, resulting in a reduced modal confinement within the waveguide core, leading to a higher optical loss. Ultimately, this leads to an increased FWHM, illustrated in Figure 4.15, which reduces the Q-factor as described in (2.14). Furthermore, increasing the reverse bias voltage improved the Q-factor and subsequently reduced the FWHM. Since more carriers were depleted from the waveguide, light in the waveguide experienced less absorption, allowing for the ring to retain light more effectively, increasing the Q-factor.

The other two important MRM properties are FSR and ER, illustrated in Figure 4.16 and Figure 4.17 respectively. The FSR appears mostly unaffected by higher reverse bias voltages, which is expected. An applied reverse bias slightly shifts the transmission dip of an optical response, resulting in a negligible change in the spacing between spectral dips. However, higher TID levels did slightly decrease the FSR. This can be attributed to the decrease in the refractive index from radiation effects, which decreases the resonant wavelengths. The ER showed a decreasing trend with increasing TID levels. This is likely due to the resonant peak shifting away from the nominal MRM operating resonant peak, which results in a reduced contrast in the resonance dip. The MRM designs with higher doping concentrations in the p-n junction region exhibited lower ER, possibly due to the optical losses present from increased carrier concentration from the higher doping level or broader resonant peaks, as seen in Figure 4.15. ER increased slightly with increasing reverse

bias voltages, following the trend of the Q-factor. This is expected because a higher Q-factor is correlated with a sharper and deeper transmission dip, which increases the ER.

The optical response from MRM design *b* is shown in Figure 4.18. The shift in the resonant dip can be observed at various TID levels. The shift from 0 Gy to 10^4 Gy is very minimal, with the spectra essentially overlapping. However, at a higher TID level of 10^6 Gy, the resonant peak experiences a blue shift around 0.2 nm. This is in agreement with (2.10) since increasing TID lowers the material refractive index, which in turn reduces the resonant wavelength.

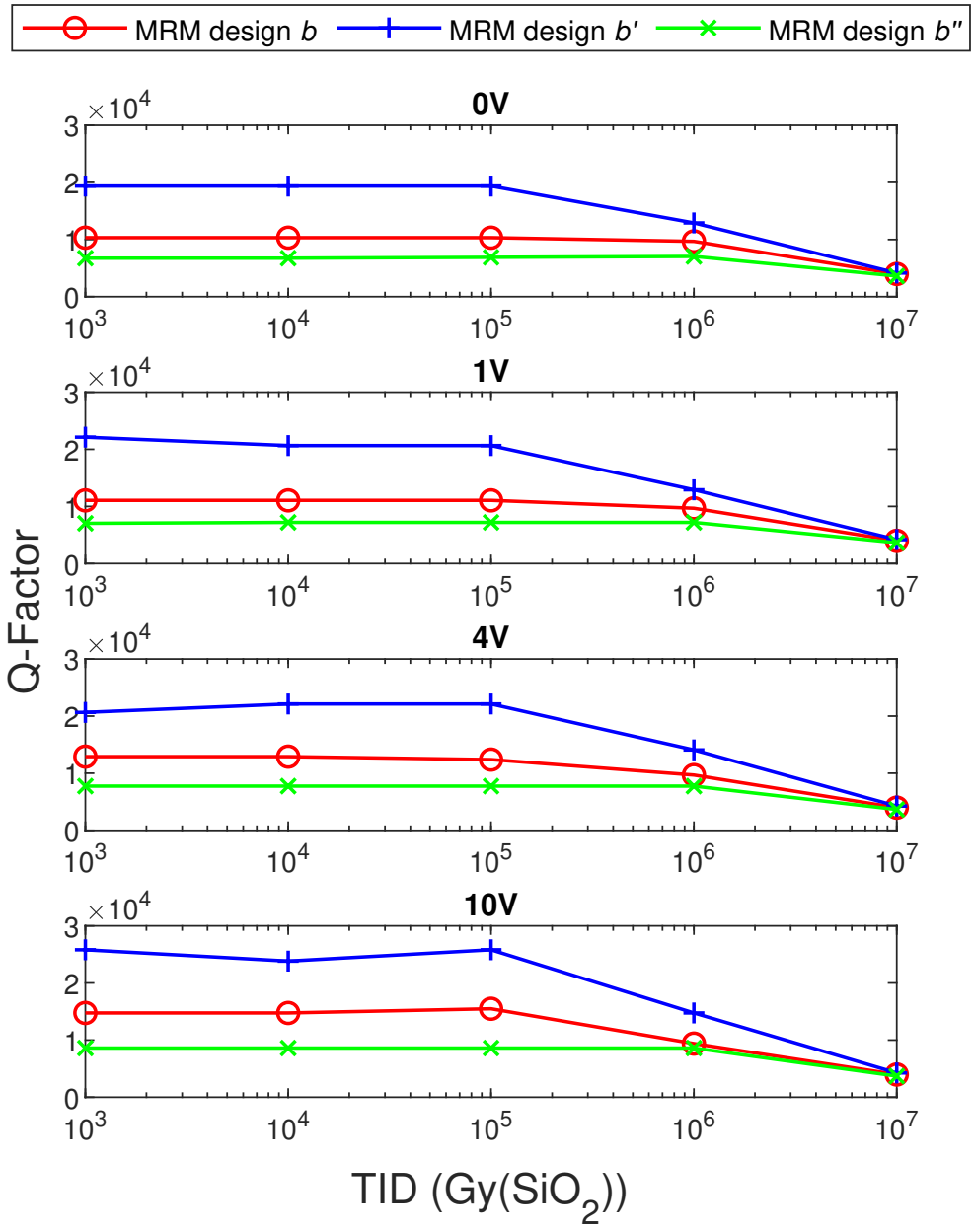

Figure 4.14: Q-factor for all MRM designs under various reverse bias voltages.

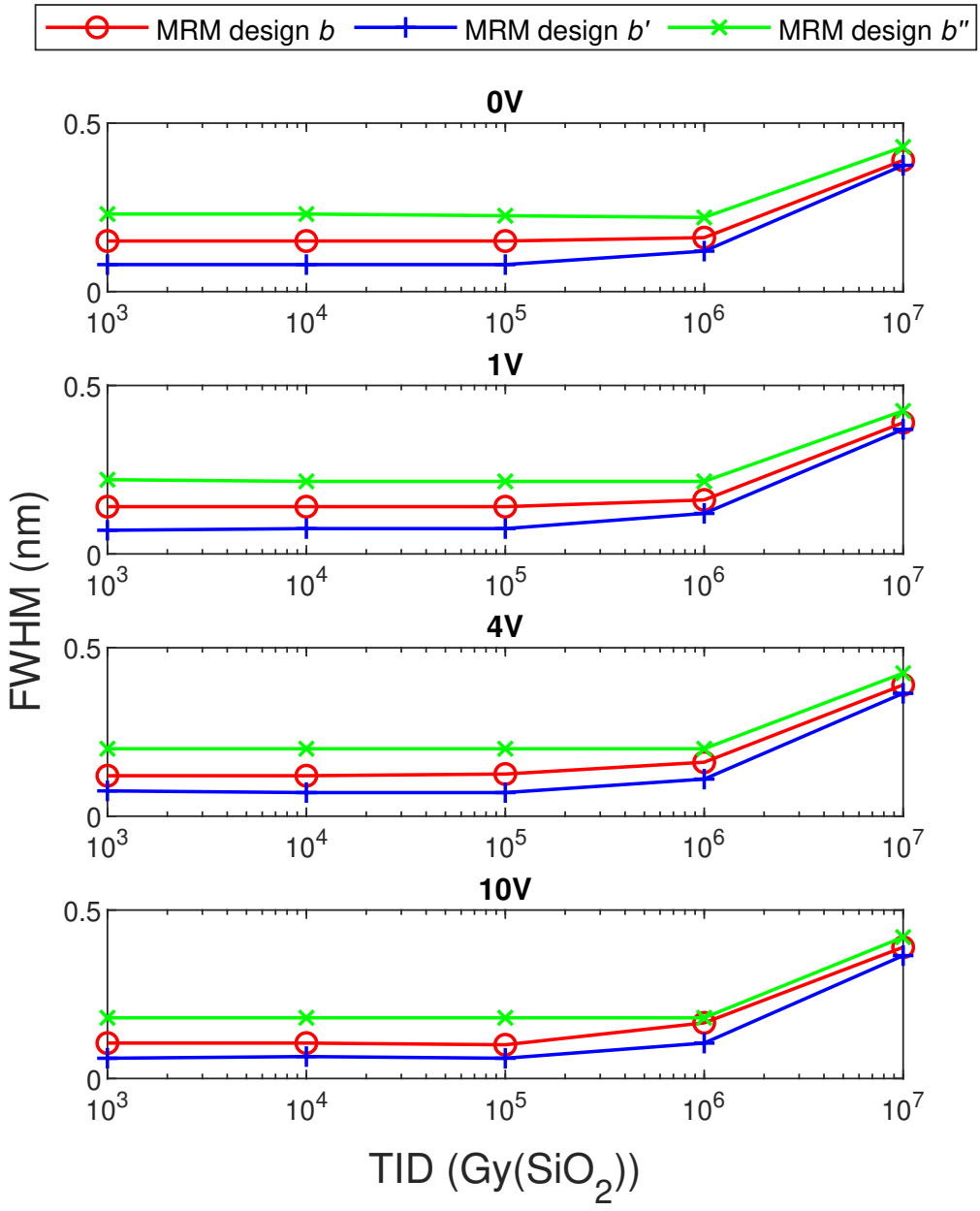

Figure 4.15: FWHM for all MRM designs at various reverse bias voltages.

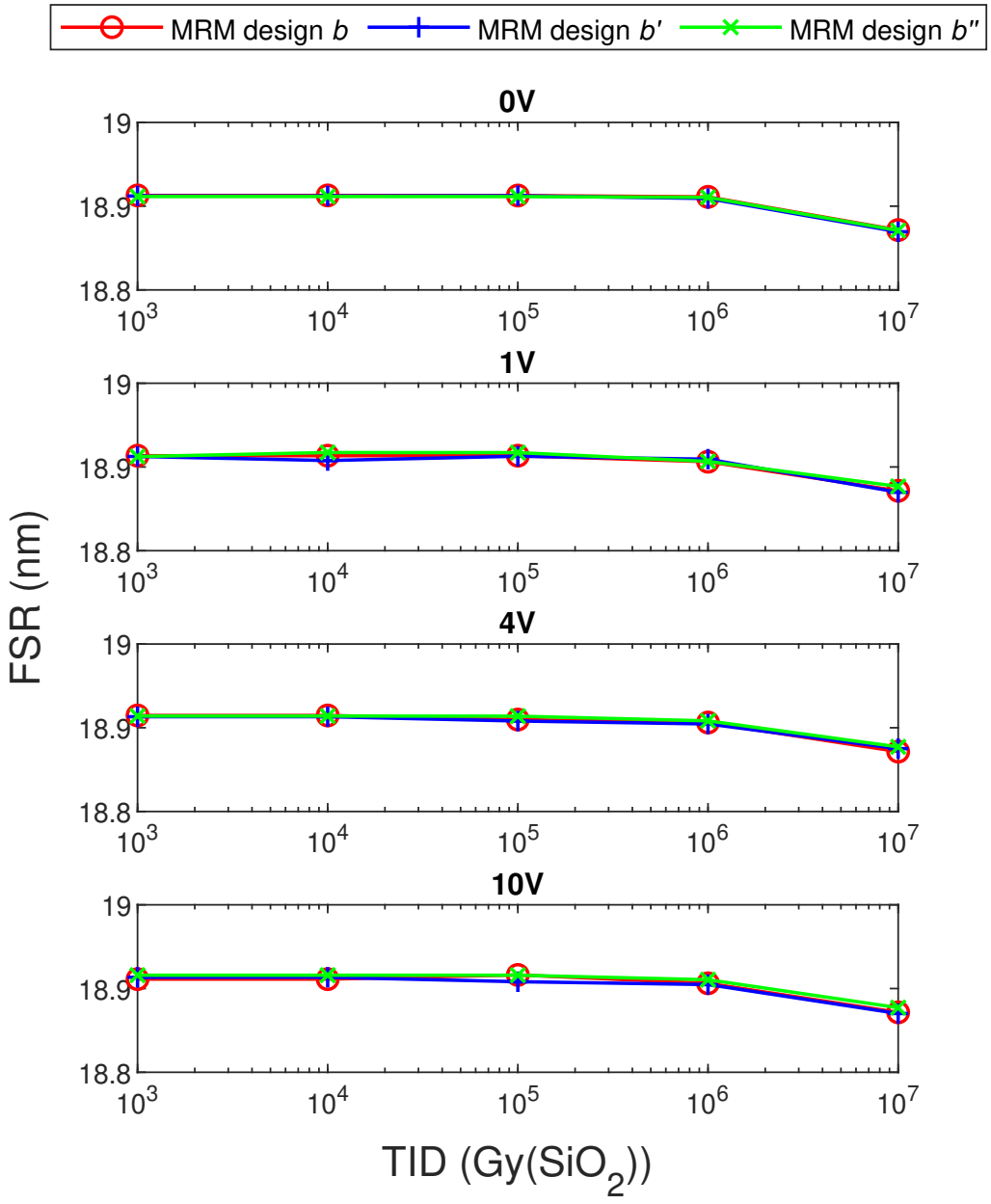

Figure 4.16: FSR for all MRM designs under various reverse bias voltages.

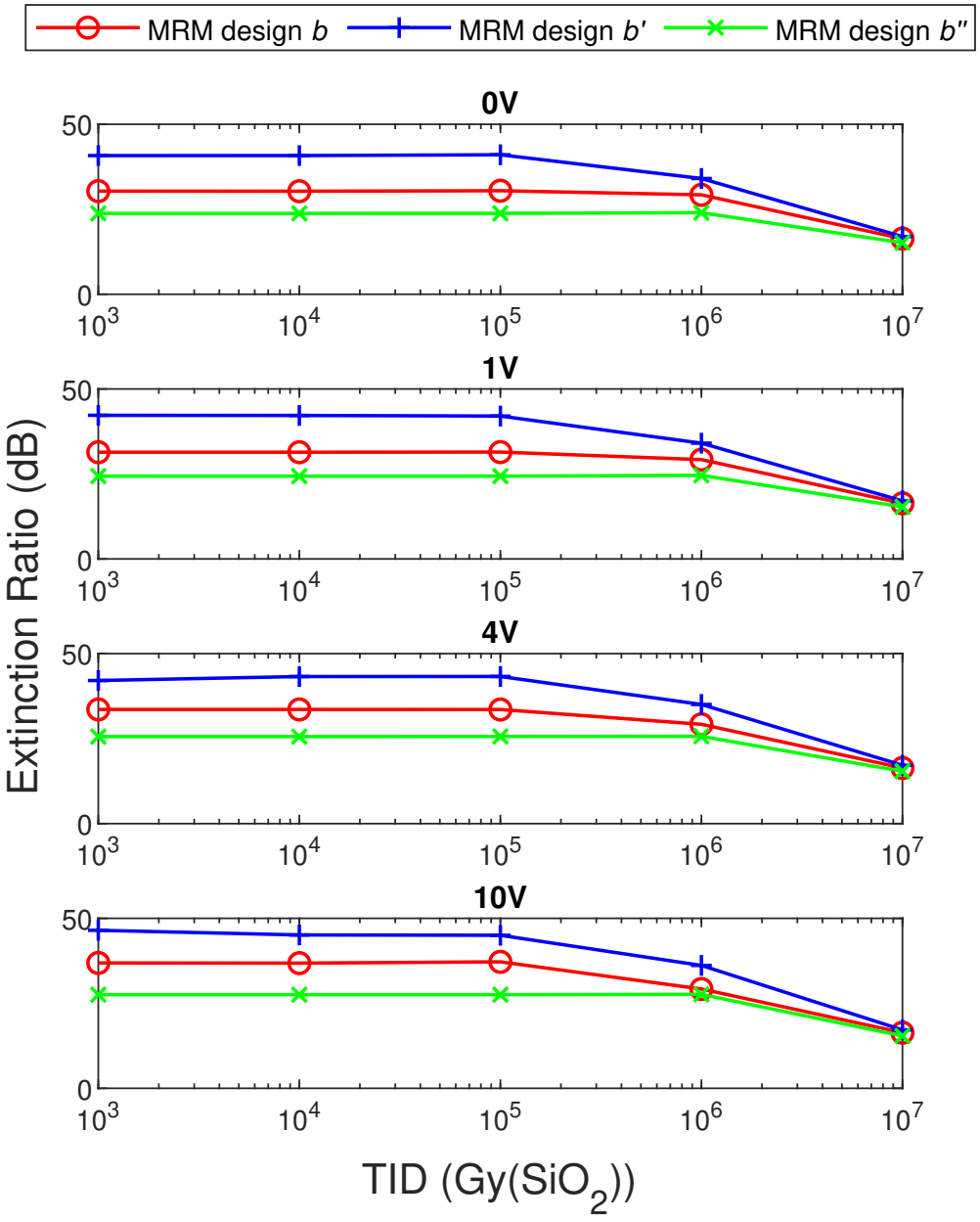

Figure 4.17: Extinction ratio for all MRM designs under various reverse bias voltages.

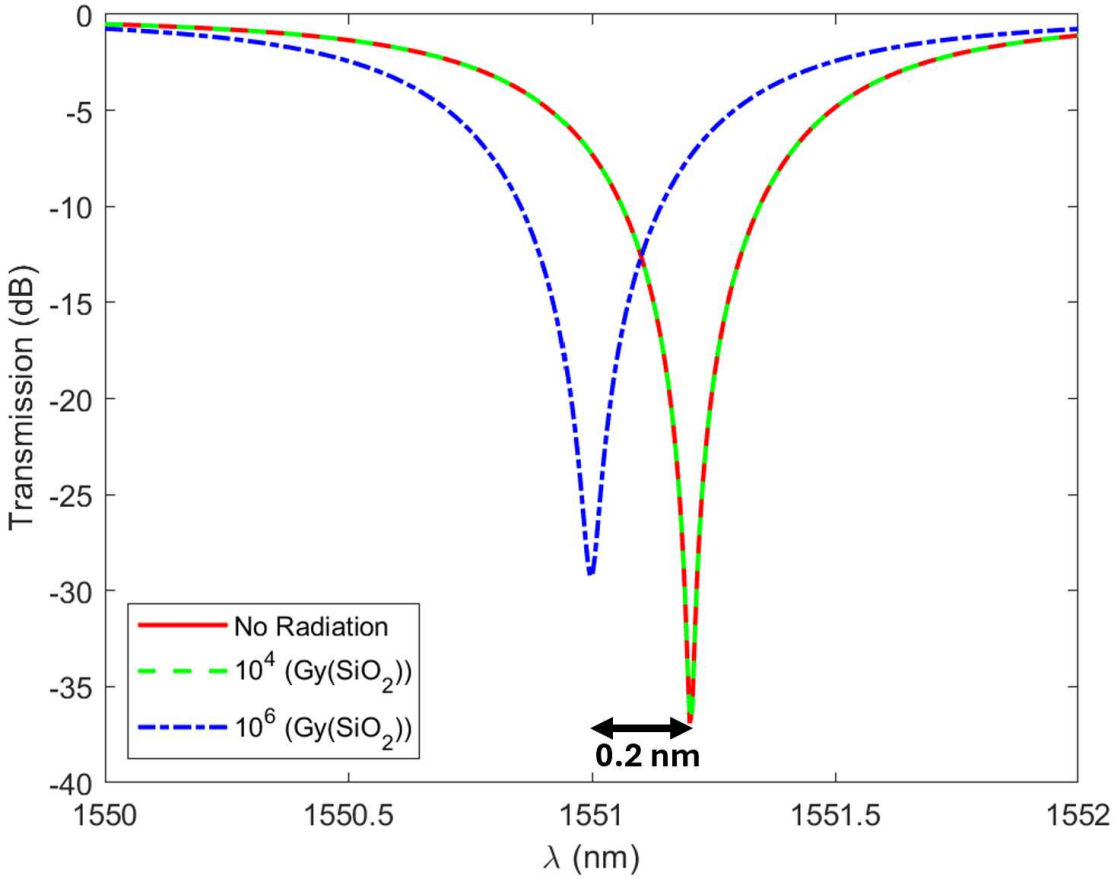

Figure 4.18: The optical response of MRM design *b* with an applied reverse bias of 10 V at various TID levels. At low TID levels, the optical response has a negligible shift; however, at higher TID levels, there is a noticeable shift of 0.2 nm.

Chapter 5

Future Work

RADPIC demonstrates promising potential with initial simulation results in reasonable agreement with experimental data. However, several areas can be improved to make RADPIC a more powerful platform by increasing accuracy and robustness. First, changes in fundamental physical processes, such as recombination velocities and the formation of trap defects in the materials, are not modeled. Including these effects could help the simulation not break down at extremely high TID levels, such as when MRM design *b'* deviated from the experimental data. Furthermore, the current method of including interface trap charge density relies on an arbitrary scaling factor to decrease the calculated value to allow for convergence in the Ansys simulation tools. Although this is practical, it limits the physical fidelity of the framework, and improving this calculation could significantly improve accuracy. In addition, the current state of RADPIC applies the refractive index change uniformly to all materials, specifically Si and SiO_2. A more accurate approach, as suggested in [22], would be to apply the refractive index changes around the boundary region, localizing radiation effects which more closely mimic the impact of trapped charge build up on the Si/SiO_2 interface. Additionally, introducing time-dependent radiation accumulation in RADPIC would likely increase accuracy in device degradation processes over the current instantaneous application of a TID level. Further enhancements could be made to RADPIC to include radiation effects from DDD and SEE, in addition to TID, to provide a more comprehensive analysis of radiation effects on SiPh devices. Although SEE events are transient and unlikely to affect the results presented in this thesis, incorporating the accumulated effects of DDD would likely have a significant impact on the findings, due to increased modifications in material properties beyond those caused by TID effects. Finally, simulating the annealing process with time and temperature effects on the devices would greatly enhance RADPIC's functionality.

Bibliography

[1] Q. Du, "High energy radiation damage on silicon photonic devices: A review," *Opt. Mater. Express*, vol. 13, no. 2, pp. 403–412, Feb 2023.

[2] M. Lalović *et al.*, "Ionizing radiation effects in silicon photonics modulators," *IEEE TNS*, vol. 69, no. 7, pp. 1521–1526, 2022.

[3] M. Zeiler *et al.*, "Radiation damage in silicon photonic Mach–Zehnder modulators and photodiodes," *IEEE TNS*, vol. 64, no. 11, pp. 2794–2801, 2017.

[4] G. N. Tzintzarov *et al.*, "Integrated silicon photonics for enabling next-generation space systems," *Photonics*, vol. 8, no. 4, 2021. [Online]. Available: https://www.mdpi.com/2304-6732/8/4/131

[5] L. Rinaldi *et al.*, "Space-grade analogue and digital photonics for satellite communications in Europe," *IEEE JLT*, vol. 42, no. 3, pp. 1004–1015, 2024.

[6] M. M. Hossen *et al.*, "Space-compliant hybrid integrated microwave photonic systems: Progress and open issues," in *MWP*, 2024, pp. 1–4.

[7] D. Mao *et al.*, "Space-qualifying silicon photonic modulators and circuits," *Science Advances*, vol. 10, no. 1, p. eadi9171, 2024. [Online]. Available: https://www.science.org/doi/abs/10.1126/sciadv.adi9171

[8] S. Bhandaru *et al.*, "Total ionizing dose effects on silicon ring resonators," *IEEE TNS*, vol. 62, no. 1, pp. 323–328, 2015.

[9] P. K. Chatterjee, S. D. Malhi, M. deWit, H. Hosack, M. G. Harward, M. M. Moslehi, and H. Hosack, "20 - integrated circuits," in *Reference Data for Engineers (Ninth Edition)*, W. M. Middleton and M. E. Van Valkenburg, Eds. Woburn: Newnes, 2002, pp. 20–1–20–113. [Online]. Available: https://www.sciencedirect.com/science/article/pii/B9780750672917500224

[10] K. Li, D. J. Thomson, L. Zhou, W. Zhang, S. Liu, W. Cao, C. G. Littlejohns, X. Yan, M. Ebert, M. Banakar, D. Tran, F. Meng, L. Wang, Z. He, F. Zhang, S. Yu, and G. T. Reed, "Beyond 300gb/s from an integrated single-channel silicon photonics modulator driver combination," in *2024 IEEE Silicon Photonics Conference (SiPhotonics)*, 2024, pp. 1–2.

[11] R. Hamerly, "The future of deep learning is photonic: Reducing the energy needs of neural networks might require computing with light," *IEEE Spectrum*, vol. 58, no. 7, pp. 30–47, 2021.

[12] R. Medina, "Photons vs. electrons [all optical network]," *IEEE Potentials*, vol. 21, no. 2, pp. 9–11, 2002.

[13] L. Chrostowski and M. Hochberg, *Silicon Photonics Design: From Devices to Systems*. Cambridge University Press, 2015.

[14] W. Bogaerts *et al.*, "Silicon microring resonators," *Laser & Photonics Reviews*, vol. 6, no. 1, pp. 47–73, 2012.

[15] R. Soref *et al.*, "Electrooptical effects in silicon," *IEEE Journal of Quantum Electronics*, vol. 23, no. 1, pp. 123–129, 1987.

[16] J. R. Schwank *et al.*, "Radiation effects in MOS oxides," *IEEE TNS*, vol. 55, no. 4, pp. 1833–1853, 2008.

[17] J. F. Ziegler, "SRIM – The Stopping and Range of Ions in Matter," Software available at http://www.srim.org, 2013, accessed: 2025-09-15.

[18] K. LaBel *et al.*, "A roadmap for nasa's radiation effects research in emerging microelectronics and photonics," in *IEEE AeroConf*, vol. 5, 2000, pp. 535–545 vol.5.

[19] N. Boynton, M. Gehl, C. Dallo, A. Pomerene, A. Starbuck, D. Hood, P. Dodd, S. Swanson, D. Trotter, C. DeRose, and A. Lentine, "Gamma radiation effects on passive silicon photonic

waveguides using phase sensitive methods," *Opt. Express*, vol. 28, no. 23, pp. 35 192–35 201, Nov 2020. [Online]. Available: https://opg.optica.org/oe/abstract.cfm?URI=oe-28-23-35192

[20] S. Grillanda *et al.*, "Gamma radiation effects on silicon photonic waveguides," *Opt. Lett.*, vol. 41, no. 13, pp. 3053–3056, Jul 2016. [Online]. Available: https://opg.optica.org/ol/abstract.cfm?URI=ol-41-13-3053

[21] S. Seif El Nasr-Storey, F. Boeuf, C. Baudot, S. Detraz, J. M. Fedeli, D. Marris-Morini, L. Olantera, G. Pezzullo, C. Sigaud, C. Soos, J. Troska, F. Vasey, L. Vivien, M. Zeiler, and M. Ziebell, "Effect of radiation on a mach–zehnder interferometer silicon modulator for hl-lhc data transmission applications," *IEEE Transactions on Nuclear Science*, vol. 62, no. 1, pp. 329–335, 2015.

[22] S. E. Nasr-Storey *et al.*, "Modeling TID effects in Mach-Zehnder interferometer silicon modulator for HL-LHC data transmission applications," *IEEE TNS*, vol. 62, no. 6, pp. 2971–2978, 2015.

[23] A. Lumerical, [Online]: https://www.ansys.com/.

[24] Ansys Lumerical, "Ring modulator," [Online]: https://optics.ansys.com/hc/en-us/articles/360042322794-Ring-Modulator. Accessed: 7/23/2025.

[25] F. B. McLean *et al.*, "Basic mechanisms of radiation effects in electronic materials and devices," Harry Diamond Labs., Adelphi, MD (USA), Tech. Rep., 09 1987.